5-2021

# Investigation of Microstructure Heterogeneity Using Multi-Length Scale Characterization of Additively Manufactured 316L SS Components for Nuclear Applications

Amy J. Godfrey
agodfre3@vols.utk.edu

To the Graduate Council:

I am submitting herewith a thesis written by Amy J. Godfrey entitled "Investigation of Microstructure Heterogeneity Using Multi-Length Scale Characterization of Additively Manufactured 316L SS Components for Nuclear Applications." I have examined the final electronic copy of this thesis for form and content and recommend that it be accepted in partial fulfillment of the requirements for the degree of Master of Science, with a major in Materials Science and Engineering.

Sudarsanam S. Babu, Major Professor

We have read this thesis and recommend its acceptance:

Suresh Baub, Eric Lass, Claudia Rawn

Accepted for the Council:
Dixie L. Thompson

Vice Provost and Dean of the Graduate School

(Original signatures are on file with official student records.)

# Investigation of Microstructure Heterogeneity Using Multi-Length Scale Characterization of Additively Manufactured 316L SS Components for Nuclear Applications:

**A Thesis Presented for the**
**Master of Science**
**Degree**
**The University of Tennessee, Knoxville**

**Amy Jordan Godfrey**
**May 2021**

# DEDICATION

To my husband, Andrew, and our daughters: Ashley, Rebecca, and Grace.

## ACKNOWLEDGEMENTS

I would like to sincerely thank:

- My committee members: Professor Suresh Babu, Professor Eric Lass, and Professor Claudia Rawn and Dr. Ryan DeHoff for their guidance and support throughout my undergraduate research work and my pursuit of a master's degree.
- Professor Suresh Babu for guiding and teaching me without reservation throughout both my undergraduate and graduate studies.
- Dr. Vincent Paquit for his support and mentorship.
- Joseph Simpson for his guidance, for writing the Emerald algorithm, and providing training and understanding of the same.
- Dr. Donovan Leonard for collecting all of the STEM/EDS data and aiding in the analysis of such.
- Dr. Michael Koehler of the Joint Institute for Advanced Materials (JIAM) Diffraction Facility, located at the University of Tennessee, Knoxville for help collecting x-ray diffraction data.
- Andres Marquez Rosy at the MDF of ORNL for training me on the scanning electron microscopes and providing endless support.
- Kevin Sisco and Sabina Kumar for their discussions and better understanding of Thermocalc analyses.
- My husband, Andrew Godfrey, for his unending help and support throughout this journey.

# ABSTRACT

Additive manufacturing allows for near net shape components to be manufactured with complex geometries and internal cooling channels while simultaneously allowing for microstructure control. Additive manufacturing has an added benefit of the possibility of removing the post processing needs associated with traditional nuclear component manufacturing. The microstructure of components built using laser powder bed fusion has been shown to be greatly affected by the build parameters. By altering the laser power, laser velocity, and the spot size the microstructure and, possibly, nanoscale partitioning may be tailored. In this study, nanoscale partitioning was confirmed to be the result of an abrupt transition of phase selection phenomenon from $\gamma$ - austenite (FCC) phase to $\delta$ - ferrite (BCC) phase when moving from the outer edge of the melt pool to the interior, center region of the melt pool. This is inferred from a distinct shift in the Cr and Ni partitioning in the inter – dendritic regions. This was achieved by studying four sample builds with varied build parameters, some of which underwent heat treatments. The samples were either built with Selective Laser Melting (SLM) or Concept Laser systems. Nanoscale partitioning was identified in samples from the build varying parameters. All sample sets were confirmed ≥ 99% $\gamma$-austenite (FCC) through X – ray diffraction. Solidification models, heat transfer models, and segmented etched optical microscopy images were performed and collected. This information, once gathered, led to the prediction of nanoscale partitioning patterns. The retained presence of nanoscale partitioning after massive transformation to ≥ 99% $\gamma$-austenite (FCC) was confirmed through STEM/EDS analysis.

# TABLE OF CONTENTS

# LIST OF TABLES

# LIST OF FIGURES

# INTRODUCTION

Metal components for nuclear applications are currently manufactured primarily by forging and casting followed by post processing procedures such as welding, hot isostatic pressing (HIP), and machining[1]. Additive manufacturing offers the ability to fabricate near net shape components with complex geometries and internal cooling features while also allowing for microstructure control [2] and the potential for less post processing needs [3]. Recent research in 316L stainless steel alloys [4, 5] suggests this microstructure and chemical partitioning control with reference to build direction may significantly change the mechanical properties, by as much as 2 – 3 times stronger in some cases. This increase in mechanical properties can impact the component performance. These changes are expected to be heterogenous within a single component. These potential benefits of additive manufacturing, however, may not be fully accepted by the nuclear industry until such components have been shown to meet all regulatory standards for their application in a nuclear setting. Recent works have shown that the microstructural characterization of “identical” parts fabricated on different printers, at different periods, different part nest, etc. may not result in “identical” properties [6, 7]. Such discrepancies in properties are the result of spatial variations of thermo – mechanical – chemical histories, which is a function of sample geometry and the scanning strategies utilized in additive manufacturing. Variations such as temperature, range from 1000 – 1800 K; thermal gradients, from $10^3$ – $10^8$ K/m; and liquid – solid interface velocities, from $10^{-3}$ – $10^0$ m/s. Thus, correlating the build parameters to the microstructural evolution and its control is of significant importance [8]. This work focuses on the multi – length scale, 2 mm – 500 nm, ex – situ characterization of additively manufactured stainless steel 316L at site specific locations to investigate the effect of build parameters on elemental partitioning and microstructural heterogeneity by utilizing advanced ex – situ characterization techniques in conjunction with theoretical computational and thermodynamic modeling [9, 10, 11]. The results presented will be of relevance for deployment of additive manufactured components for a wide range of use in nuclear energy applications [12].

# CHAPTER 1 BACKGROUND AND LITERATURE REVIEW

This chapter will explore information on the background of processes and previously published works available in literature that are of relevance to this work.

## 1.1 Metal Additive Manufacturing – Powder Bed Fusion

Powder bed fusion (PBF) is one type of metal additive manufacturing, wherein a metal powder feedstock is spread evenly across a metal substrate, called a build plate. The powder is then melted in accordance with a specified geometry. The melting of the powder is accomplished with a laser, either continuous or pulsed, or an electron beam. The laser power is typically in the range of 200 – 400 W. The specified geometry is then divided into layers and the laser will melt the powder layer – wise according to the specified geometry [3]. After a layer is melted another layer of powder is added evenly through the use of a re – coater blade. The specified geometry is built in this layer – wise fashion until the part is finished.

The laser powder bed fusion (L – PBF) process creates melt pools whose size, solidification model, and thermal gradient are dependent upon the input parameters, properties of the metal, part geometry, and scan pattern. This dependency leads to spatial variations of thermo-mechanical-chemical histories, which is a function of both sample geometry and scanning strategies utilized in additive manufacturing. Previous work has shown that such spatial variations of microstructure and defects do have an impact on the mechanical properties of an additively manufactured component, thus a better understanding is warranted to correlate these microstructure variations and our control of them.

## 1.2 Previous Work on Heterogeneity of AM SS Microstructures

Much research has been done to investigate the microstructure of stainless steel that results from additive manufacturing through L – PBF[5, 12, 13, 14]. Wang et. al. found increased strength (2 – 3 times) and ductility over traditional as – cast and wrought stainless steel samples. Additionally, distinct hierarchical microstructures were discovered in the AM stainless steel samples. In this study, samples were fabricated on two different continuous L – PBF machines: a Concept laser system and a Fraunhoffer system. These samples were found to

be ≥ 97% γ-austenite (FCC) with little to no δ-ferrite (BCC). Multi – length scale characterization, from 200 μm to 200 nm, revealed a microstructure with distinct cellular solidification structures and chemical heterogeneity. Chemical heterogeneity occurs when the chemical composition is not found to be homogeneous; in the case of this study Cr and Mo partitioning were found. These cellular structures also contained high dislocation density at the cell walls, as well as nano – oxide inclusions, in the form of Mn-Si-O, that were predominantly segregated to the cell walls. The marked increase in strength, 2 – 3 times as strong, and ductility over traditionally cast and wrought samples of similar composition was solely attributed to this high dislocation density at the cell walls. Elemental partitioning of Cr and Mo at the cell walls was also found as would be expected with γ-austenite (FCC) solidification, however there were no further partitioning studies performed as the samples were found to be ≥ 97% γ-austenite (FCC).

## 1.3 Previous Work on Microstructure and Mechanical Properties

Research has been conducted and previously published regarding the connection between porosity and hot isostatic pressing with solution anneal (HIP/SA) on mechanical properties of additively manufactured stainless steel [12, 13] with respect to nuclear applications. In this study samples were printed on a pulse L – PBF printer with engineered, or intentional, porosity of sizes from . Tensile samples were milled and tested from all degrees of porosity in as – built and HIP/SA condition. All samples, including those with the greatest percentage and largest porosity, met or exceeded required nuclear regulatory committee (NRC) standards. The results confirmed that HIP/SA proved sufficient to minimize any scatter in properties of 316L stainless steel that was additively manufactured, even though fractography analyses revealed some porosities remained open. The porosities that did not heal during HIP/SA, however, had no significant deleterious effect on the properties. This proves that implementation of additively manufactured components in a nuclear environment could meet the properties required in NRC standards.

Further studies were performed to investigate the microstructure. These studies began with the predicting the distribution of thermal gradients in the range of $10^4$ to $10^8$ K/m and a range of liquid – solid interface velocities of $10^{-2}$ to $10^1$ m/s acquired from heat transfer models. In the case of low liquid – solid velocity (<

$10^{-3}$ m/s), typical welding solidification and microstructure may occur, wherein the liquid would solidify as $\delta$-ferrite (BCC). High liquid – solid velocities, > $10^{-3}$ m/s, would lead to solidification as $\gamma$-austenite (FCC). Both cases are found in the EBSD images. Spinel oxide, $MnSiO_2$, formation was predicted from Scheil – Gulliver solidification models as well as inter – dendritic nano – scale partitioning of Si, Mo, and S. Such oxides and partitioning are also found in literature. Tensile elongation was greatly affected as a result of the spatial distribution of the defects as was predicted by deformation models.

## 1.4 Solidification of 316L Stainless Steel

Additive manufacturing, L – PBF, of metals shares many similarities to traditional fusion welding. In both AM and traditional welding localized melting is brought about by a mobile heat source to create a continuous piece or part. Thus, traditional welding literature can be referenced to inform on and understand a large portion of the science that dictates the solidification path of additively manufactured metals. It has been well researched and proven that the two main influences in the solidification mode of a given stainless steel are: chemical composition and the solidification rate of the melted region. Both of these influences can be described empirically as well as theoretically through equations and modelling such as the interface response function (IRF) [19, 22]. Solidification of stainless steels may occur as $\delta$-ferrite (BCC), $\gamma$-austenite (FCC), or as a combination of some type containing both phases.

### *1.4.1 Chemical Composition*

As previously mentioned, solidification of stainless steels may occur as $\delta$-ferrite (BCC), $\gamma$-austenite (FCC), or as a combination of some type containing both phases. While additional phases (such as martensite or other precipitation hardened phases) may be brought about with additional heat treatments or through rapid cooling methods, this section on chemical composition will focus solely on compositional effects on the phase fractions of $\delta$-ferrite (BCC)/$\gamma$-austenite (FCC) in stainless steels. Metallurgical process maps were developed to aid in the predictions of phase fractions for any given steel alloy [23]. The most widely accepted of these process maps for stainless steels with < 1% Si are the WRC – 1992, Figure 1, and the Schaeffler, Figure 2, diagrams. These process

maps plot the Ni equivalent vs the Cr equivalent, however, each plot utilizes slightly different equations for calculation these equivalences. The WRC – 1992 plot uses the equations listed on the plot for $Cr_{eq}$ = Cr + Mo + 0.7Nb and $Ni_{eq}$ = Ni + 35C + 20N + 0.25Cu. The red star marks the value for the primary composition studied throughout this work with $Cr_{eq}$ = 19.24 and $Ni_{eq}$ = 12.16. The Schaeffler diagram, Figure 2, uses the equations listed on the plot for $Cr_{eq}$ = Cr + Mo + 1.5Si + 0.5Nb and $Ni_{eq}$ = Ni + 30C + 0.5Mn. The red star marks the value for the primary composition studied throughout this work with $Cr_{eq}$ = 19.78 and $Ni_{eq}$ = 12.45.

The WRC – 1992 plot predicts FA (ferrite followed by austenite) solidification for this primary composition while the Schaeffler plot predicts A+F (austenite then ferrite) solidification for this primary composition. It is important to note that the WRC – 1992 process was developed from traditional welding data which means with a slow cooling rate on the order of $10^3$ K/s, however, AM produces an average cooling rate that is an order of magnitude higher at $10^4$ K/s. Thus, the WRC – 1992 may not be entirely accurate under these settings. The actual findings for this study will discussed in detail in the Results & Discussion section.

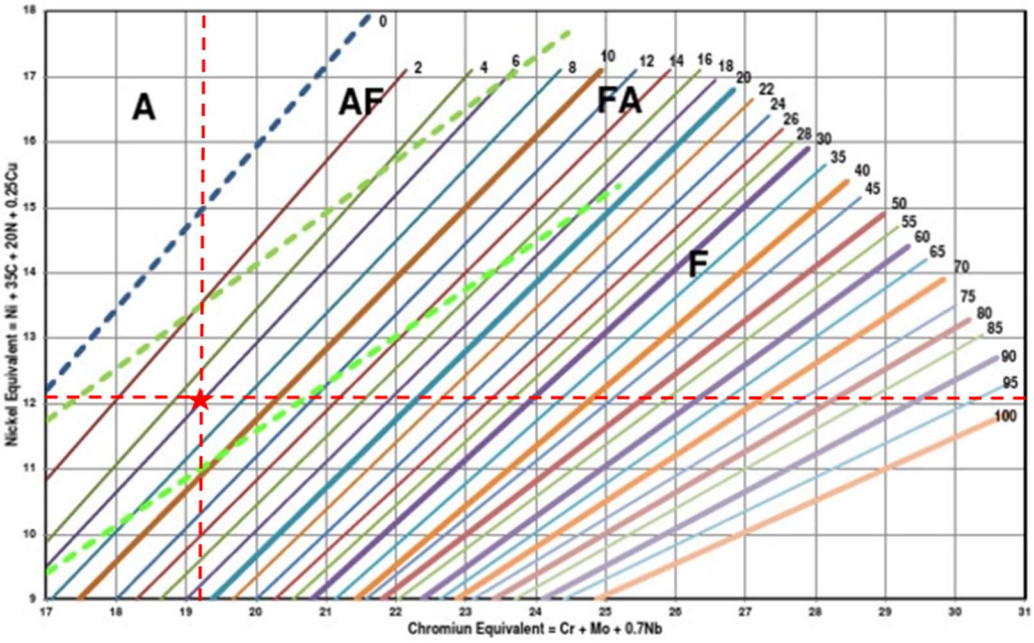


**Figure 1: WRC – 1992 process map. The red star marks the primary composition for this study.**

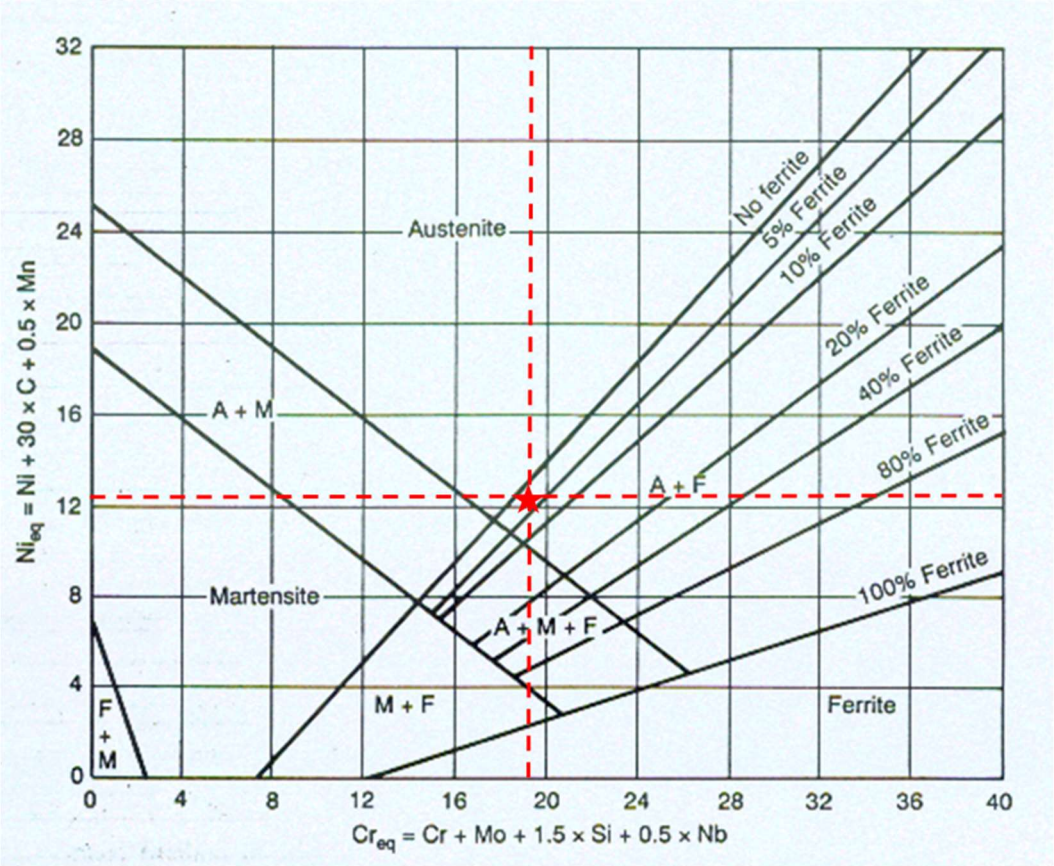


**Figure 2: Schaeffler diagram with the red star marking the primary composition for this study.**

### *1.4.2 Solidification Rate*

Solidification modes may change under rapid cooling rates such as those found in additive manufacturing. This rapid solidification results in a much different microstructure as well as altered partitioning patterns than those found with slower solidification rates [16]. Experiments into the effect of cooling rate, varied from $10^{-1}$ – $10^{8}$ K/s, on different stainless steel alloys [28] revealed five distinct solidification modes: 1 – single – phase austenite (A), 2 – primary austenite followed by second – phase ferrite (AF), 3 – eutectic ferrite in conjunction with eutectic austenite (E), 4 – primary ferrite followed by second – phase austenite (FA), and 5 – single – phase ferrite (F).

### *1.4.3 Interface Response Function*

Solidification modes for a given alloy system can also be predicted through theoretical equations. One such system of theoretical equations, that correlated the effects of dendrite tip radius, solid/liquid interface, and primary dendrite arm spacing, was developed by Kurz, Giovanola, and Trivedi. Their work became known as the KGT model for directional solidification [17] and may be applied in systems with high growth velocities. This model, which may also be referred to as the Interface Response Function (IRF), enabled the prediction of which phase would solidify when as well as microstructural features that could be found in each type of solidification. This model is comprised of the following equations: These equations may be iteratively solved with appropriate inputs to predict the primary solidification phase, which will be the phase that achieves the highest either dendrite tip temperature or planar temperature at a given growth velocity. Velocity dependent partition coefficient:

$$k_V^i = \frac{k_o^i + a_o\left({V_S}/{D_i}\right)}{1 + a_o\left({V_S}/{D_i}\right)}$$

Velocity dependent liquidus slope:

$$m_V^i = m_o^i\left[\frac{1 - k_V^i\left(1 - ln\left\{{k_V^i}/{k_o^i}\right\}\right)}{1 - k_o^i}\right]$$

Dendrite tip liquid concentration:

$$c_l^{i*} = \frac{c_o^i}{1 - \left(1 - k_V^i\right) Iv\{Pe^i\}}$$

Dendrite tip temperature:

$$T_d = T_l + \sum_i \left(c_l^{i*} m_V^i - c_o^i m_o^i\right) - \frac{2\Gamma}{R} - \frac{V_S}{\mu} - \frac{GD}{V_S}$$

Planar front temperature:

$$T_{planar} = T_s + \sum_i c_o^i \left(\frac{m_V^i}{k_V^i} - \frac{m_o^i}{k_o^i}\right) - \frac{V_S}{\mu}$$

where $k_o^i$ is the equilibrium partition coefficient for element $i$, $a_o$ is the characteristic diffusion distance, $V_S$is the solid – liquid interface velocity, $D_i$ is the solute diffusivity of element $i$, $m_o^i$ is the equilibrium liquidus slope of element $i$, $c_o^i$is the liquid equilibrium concentration of alloy element $i$, $Pe^i$ is the Peclet number for element $i$, $Iv\{Pe^i\}$ is the Ivanstov function, $T_l$ is the liquidus temperature of the original alloy composition, $\Gamma$ is the Gibbs – Thomson coefficient, and $\mu$ is the interface kinetic coefficient. The KGT/IRF will be of significant importance to this study.

### *1.4.4 δ/γ Phase Transformations in Stainless Steels*

Again, solidification of stainless steels may occur as δ-ferrite (BCC), γ-austenite (FCC), or as a combination of some type containing both phases. However, phase transformations from δ-ferrite (BCC) to γ-austenite (FCC) are also possible. Such phase transformations have been researched and shown to be brought about by one of three modes: 1 – slow cooling diffusional transformation, 2 – “diffusionless” peritectic transformation, or 3 – “diffusionless” massive transformation. Research has been conducted into the δ-ferrite (BCC) to γ-austenite (FCC) phase transformation phenomena [24, 25]. These studies utilized high – temperature microscopy to investigate the δ-ferrite (BCC) to γ-austenite (FCC) phase transformation of steels of peritectic compositions. Peritectic reactions happen as a two – stage process: 1 – Liquid + $\delta \rightarrow \gamma$,

followed by 2 – $\delta \rightarrow \gamma$ and Liquid $\rightarrow \gamma$. This allowed the researchers to look into rapid cooling rates, which has previously been discussed as having a significant effect on solidification. Such rapid cooling rates revealed a massive "diffusionless" transformation instead of the expected diffusional transformation. In fact, massive "diffusionless" transformation was found to occur when cooling rates exceeded a threshold of 1200 K/s, which is well below the solidification rates of ~$10^4$ K/s in the study to be discussed herein. This massive transformation resulted in significant and increasing elemental partitioning ahead of the Liquid/$\delta$ interface with an increasing cooling rate.

### *1.4.5 Previous Work on Solidification Modes*

Previously published work by Galicki et. al. [14] revealed spatter particles inherent to the L – PBF process were found to have solidified as single crystal BCC stainless steel. Rapid solidification velocities (> 1 m/s) were discovered which may allow for both planar solidification and solute trapping. An interface response function (IRF) model was utilized to predict solidification through dendritic BCC growth at low solidification rates and, conversely, planar BCC solidification was predicted at high solidification rates. The spatter particles were also found to have an outer oxidation layer. However, nucleation kinetics suggests that some droplets may have been lacking in oxide nucleation sites allowing for sufficient supercooling to lead to the discovered metastable BCC dominance. It was noted that these BCC spatter particles exhibited an oxide shell which could lead to sufficient undercooling to temperatures to make it possible for heterogeneous nucleation of BCC to win out over the thermodynamically stable FCC phase.

## 1.5 Background Summary

The literature review, in addition to works listed in Table 1, establishes the direct correlation of print parameters, microstructure, and mechanical properties. Print parameters have been shown to have a significant impact on thermal gradients and solidification velocities and the resultant microstructure of an additively manufactured component. This resultant microstructure in turn directly effects the mechanical properties of a printed component.

**Table 1: Summary of Published Research Related to AM.**

| Topic | Research Directions and Findings | References |
|---|---|---|
| AM for Nuclear Applications | literature relevant to use of AM components in a nuclear environment | Refs. 1 |
| Process Parameter and Microstructure Control | direct correlation between processing parameters and resultant microstructures | Refs. 2, 5, 7, 8, 9, 17, 28 |
| Process Parameter and Mechanical Behavior | direct correlation between processing parameters and mechanical properties | Refs. 4, 10, 15, 29 |
| Solidification and the Effect of Cooling Rate | effect of cooling rate on solidification velocities and modes | Refs. 16, 20, 26, 27 |
| Thermodynamic and Heat Transfer Modelling | using analytical and thermodynamic models for microstructure and solidification mode rationalization and optimization | Refs. 11, 19 |
| Phase Selection and Phase Transformations | modelling and characterization used to identify solidification modes | Refs. 14, 22 - 25 |
| Characterization and Qualification | utilizing multi-length scale characterization techniques to inform qualification of parts | Refs. 6, 12, 13, 18 |
| Radiation Effects on Additively Manufactured Components | Effect of Cr migration to grain boundaries shown to worsen IASCC | Refs. 30, 31 |

Additive manufacturing has also been shown to have thermal gradients and solidification velocities that have a significant impact on solidification modes of 316L stainless steel. Additionally, the theoretical equations discussed here have established confidence in the validity of predictions that may be gleaned from iterative solutions of the same. Thus, the current literature review supports the theory that controlling print parameters may aid in tailoring an additively manufactured components mechanical properties and service life; as well as the ability to accurately predict the expected solidification model.

## 1.6 Present Investigation

A clear and direct correlation between print parameters, microstructure, and mechanical properties has been thoroughly established with the print parameters leading to the cascade of effects: change in parameters – change in thermal gradients and solidification velocities – microstructural changes – altered mechanical properties. AM also has the unique ability to offer simultaneous benefits for the fabrication of components for use in nuclear applications. These benefits include the potential to produce near net components with complex geometries and internal cooling features that have previously been challenging to create; rapid iterative abilities that can significantly speed optimization of components; and the potential for microstructural control. These benefits could reduce waste and manufacturing time over the current manufacturing technologies for metal nuclear components which consists of forging/casting and machining. However, any component that will considered for use in nuclear applications must meet all industry and regulatory standards.

### *1.6.1 Objectives*

The goal of this investigation was to investigate and determine the cause of a distinct and interesting microstructural contrast originally discovered within an AM build designed to study the effect of varying build parameters on porosity formation. This discovery of contrast changes led to a total of four builds to be included in the study.

### *1.6.1 Knowledge Base Gaps*

While much research has been conducted into metal AM, there still exists avenues for further research. For example, the correlation of build parameters on microstructural evolution, mechanical properties, and porosity formation has been well documented [5, 9, 13, 14, 16, 18, 19, 28]. There have also been effective studies on the effect of post fabrication heat treatments on both porosity and mechanical properties. Previous studies have even revealed elemental partitioning in AM components. However, there is still a gap in the research of this elemental partitioning, its causes, and its resulting effects on the overall component.

### *1.6.1 Approach*

This research study incorporates samples from four distinct 316L stainless steel AM builds: two builds from a pulse laser system and two builds from a continuous laser system. All samples were built at the Manufacturing Demonstration Facility of Oak Ridge National Laboratory. All samples were investigated to discover whether the final room temperature structure was $\delta$-ferrite (BCC), $\gamma$-austenite (FCC), or as a combination of some type containing both phases. One sample was selected for a comprehensive multi – length scale characterization that also investigated inter – dendritic elemental partitioning. Chapter 2 details all experimental procedures and data collection parameters. All builds are detailed in this chapter. All characterization techniques utilized in the data collection are also outlined in this chapter. Results and discussion are fully detailed in Chapter 3. This begins with the discovery of the aforementioned distinct microstructural contrast, an initial investigation and corresponding hypothesis. The results of the initial investigation led to a revised hypothesis followed by detailed characterization, theoretical modelling, and thermodynamic modelling. Chapter 4 describes available avenues for future work of this study. A summary of the results and concepts of this study may be found in Chapter 5. These concepts primarily relate to the solidification path and elemental partitioning found in AM 316L stainless-steel and the effect of varying build parameters and print system on the final room temperature structure of AM 316L stainless steel components.

# CHAPTER 2 EXPERIMENTAL PROCEDURES & DATA COLLECTION

Four builds were investigated in total for this study. Samples from each build were sectioned and mounted in the xz direction Figure 3, before polishing and/or etching dependent upon the next characterization method to be performed. The complete weld pool morphology can be seen in Figure 4. The xz direction was selected to enable more accurate capture of all regions of a weld pool, including the weld pool edge and interior. The xy direction was determined to have the potential for conflicting effects of overlapping weld pools and re – melt. Taking a thin film in the xy direction would have the potential to sample through multiple weld pools, thus “muddying” any results. These mounted samples were then characterized using optical microscopy, electron backscatter diffraction (EBSD), and X – ray diffraction (XRD). Additionally, a representative sample from the parameter study build was characterized with scanning electron microscopy with energy dispersive x – ray spectrometry (STEM/EDS).

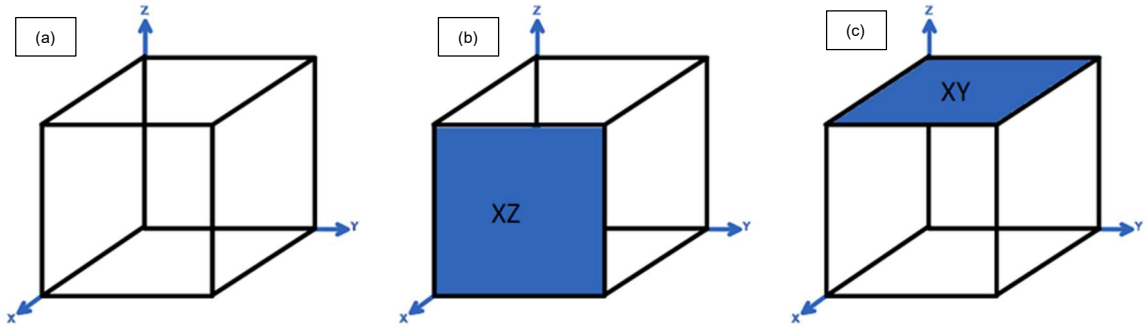


**Figure 3: Illustration of (a) simple cubic, (b) xz plane highlighted in blue, and (c) xy plane highlighted in blue for reference.**

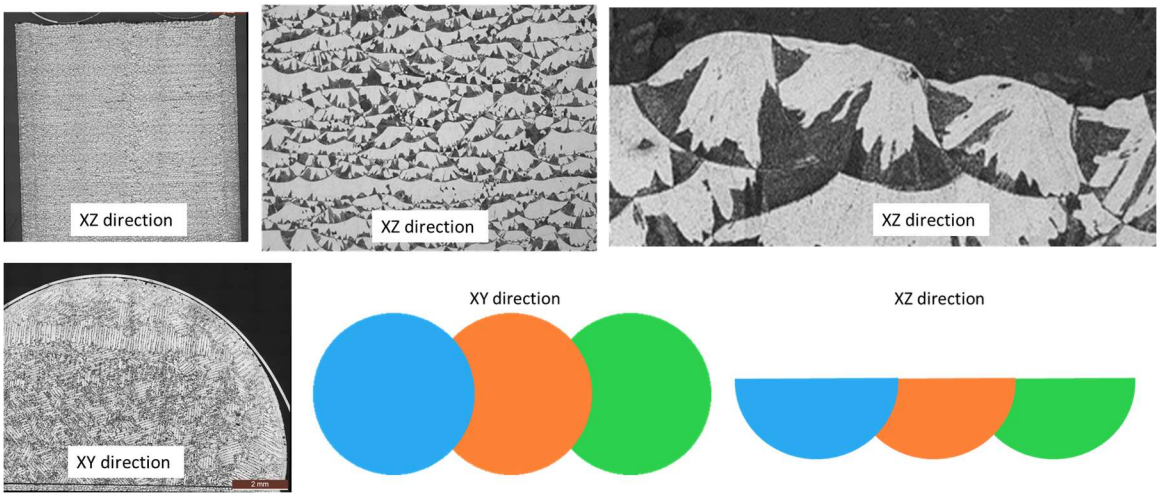


**Figure 4: Sectioned and mounted weld pool morphology in xz and xy directions; and 3D models of xy versus xz direction. Ref: Unpublished research by Simpson et al.**

## 2.1 Builds

### *2.1.1 Parameter Study*

The first sample set, to be referred to as the parameter study, was built on the M2 concept laser printer at the MDF and consisted of 29 cubes built at varying laser powers, laser speeds, and spot sizes. A Binx – Binky randomization was used to achieve a randomized distribution of power from 200 Watts – 290 Watts – 380 Watts; with velocities from 800 mm/s – 1200 mm/s – 1600 mm/s; with trace widths of 70 μm – 110 μm – 150 μm; and with spot sizes of 50 μm – 125 μm – 200 μm across the 29 – sample set, as seen in Figure 5.

This build was initially designed as an experiment to investigate and correlate the effect of varying build parameters to porosity formation within a part. Sample 11 was found to have the lowest percentage of porosity, 0.05%, while sample 1 had the most, 21.33%. The graph, Figure 5, shows the variance in build parameters and is colored in a gradient scale corresponding to the percentage of relative porosity with the lowest porosity in green transitioning to the highest in red. The complete list of relative porosity is represented in Table 2. This build also served as the impetus for this study due to an interesting discovery seen in an etched optical micrograph.

Several etchants were investigated to best reveal both the microstructure and porosity of parts fabricated in the parameter study build in order to segment etched optical images for quantification and identification of different types of pores associated with additive manufacturing. The etchant, a standard for welding, was chosen and etching was conducted with 10g oxalic acid dissolved in 100ml distilled water by electrolytically etching at 50-60mA for 6 minutes. Etching revealed an interesting and stark contrast in microstructure, see Figure 6. This leads to a question, could solidification mode differences cause such a contrast difference? Additionally, what are the different available solidification modes for 316L stainless steel, and can they be confirmed?

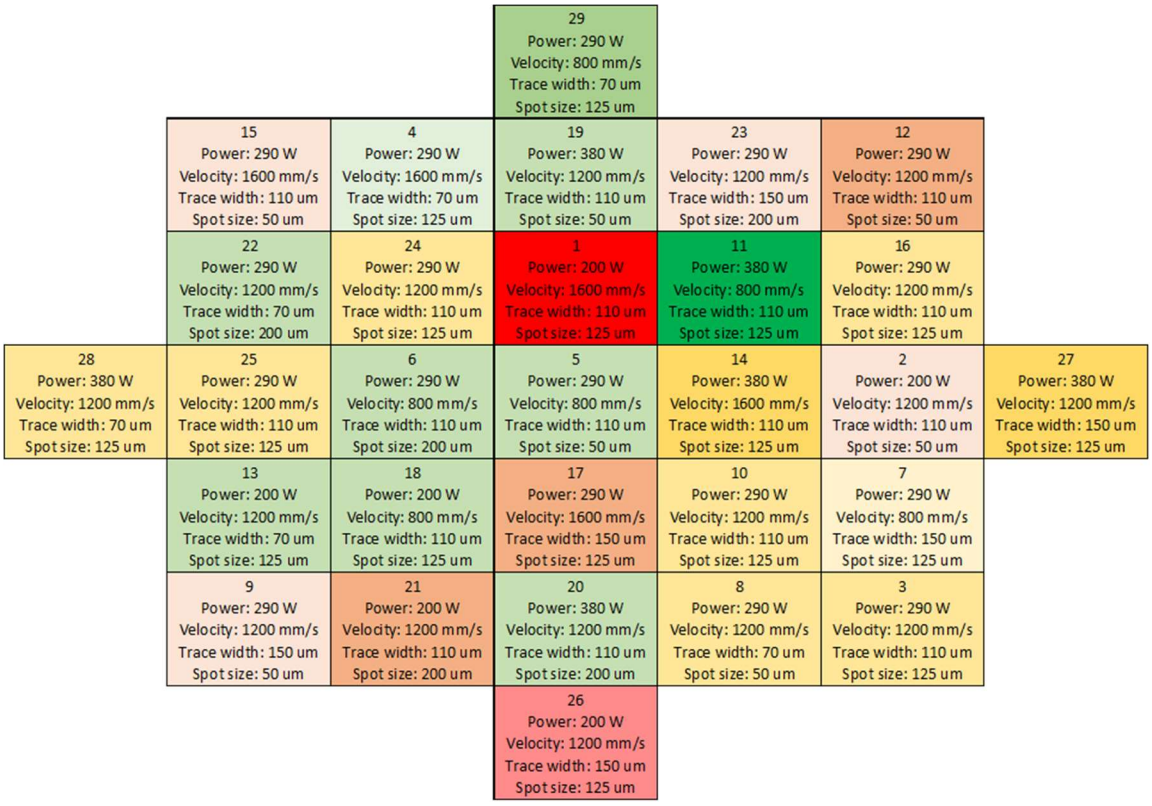


**Figure 5: Parameter study build of 29 samples. Gradient shows variance in relative porosity from least porosity (green) to most porosity (red). Ref: Unpublished research by Simpson et al.**

**Table 2: Parameter study build table of parameters and relative porosity. Gradient scale from lowest porosity in green to highest in red.**

| Sample # | Power(W) | Velocity (mm/s) | Trace Width (um) | Spot Size (um) | Relative Porosity (%) |
|---|---|---|---|---|---|
| 1 | 200.0 | 1600.0 | 110.0 | 125.0 | 21.326 |
| 2 | 200.0 | 1200.0 | 110.0 | 50.0 | 8.267 |
| 3 | 290.0 | 1200.0 | 110.0 | 125.0 | 1.008 |
| 4 | 290.0 | 1600.0 | 70.0 | 125.0 | 0.67 |
| 5 | 290.0 | 800.0 | 110.0 | 50.0 | 0.485 |
| 6 | 290.0 | 800.0 | 110.0 | 200.0 | 0.225 |
| 7 | 290.0 | 800.0 | 150.0 | 125.0 | 0.773 |
| 8 | 290.0 | 1200.0 | 70.0 | 50.0 | 1.39 |
| 9 | 290.0 | 1200.0 | 150.0 | 50.0 | 6.916 |
| 10 | 290.0 | 1200.0 | 110.0 | 125.0 | 0.997 |
| 11 | 380.0 | 800.0 | 110.0 | 125.0 | 0.05 |
| 12 | 290.0 | 1600.0 | 110.0 | 50.0 | 12.633 |
| 13 | 200.0 | 1200.0 | 70.0 | 125.0 | 0.234 |
| 14 | 380.0 | 1600.0 | 110.0 | 125.0 | 2.263 |
| 15 | 290.0 | 1600.0 | 110.0 | 200.0 | 7.223 |
| 16 | 290.0 | 1200.0 | 110.0 | 125.0 | 1.063 |
| 17 | 290.0 | 1600.0 | 150.0 | 125.0 | 14.321 |
| 18 | 200.0 | 800.0 | 110.0 | 125.0 | 0.346 |
| 19 | 380.0 | 1200.0 | 110.0 | 50.0 | 0.283 |
| 20 | 380.0 | 1200.0 | 110.0 | 200.0 | 0.441 |
| 21 | 200.0 | 1200.0 | 110.0 | 200.0 | 11.253 |
| 22 | 290.0 | 1200.0 | 70.0 | 200.0 | 0.346 |
| 23 | 290.0 | 1200.0 | 150.0 | 200.0 | 9.945 |
| 24 | 290.0 | 1200.0 | 110.0 | 125.0 | 1.202 |
| 25 | 290.0 | 1200.0 | 110.0 | 125.0 | 1.095 |
| 26 | 200.0 | 1200.0 | 150.0 | 125.0 | 19.636 |
| 27 | 380.0 | 1200.0 | 150.0 | 125.0 | 2.019 |
| 28 | 380.0 | 1200.0 | 70.0 | 125.0 | 0.832 |
| 29 | 290.0 | 800.0 | 70.0 | 125.0 | 0.121 |

**Figure 6: Etched optical micrograph of sample 6 of the parameter study build revealing stark etching contrast. Ref: Unpublished research by Simpson et al.**

### *2.1.2 Tensile Heat Treatment Study*

The second sample set was also built on the M2 concept laser printer at the MDF and will be referred to as the tensile heat treatment study. The tensile heat treatment sample set was built using the standard print parameters for the M2 concept laser printer of 370 Watts, 1350 mm/s velocity, 130 µm spot size, and 90 µm hatch spacing. The build consisted of 20 cylindrical samples with the following dimensions: 13 mm diameter x 65 mm long.

The initial experiment, again performed as part of the TCR project, was designed to investigate the correlation of the effects of different heat treatments, different cooling rates, and HIP on the mechanical properties of an AM component. The samples were subjected to the heat treatments listed in Table 3, with 4 samples included for each heat treatment. Tensile tests were performed on the samples and the results were previously published [29]. To summarize, all samples subjected to heat treatments were found to exceed the requirements of the ASTM F3184 – 16 tensile property standards, thus providing evidence that tensile properties should not be a concern for AM components in consideration for use in nuclear applications.

### *2.1.3 Layer Time Experiment Study*

The third sample set was built on the Renishaw SLM printer at the MDF and will be referred to as the LTE build. This sample set was initially printed as a part of an EPRI & DOE project studying the effect of “layer – time” on the defect formation in a build, Figure 7. The Renishaw printer is a pulse laser printer which can lead much different temporal and spatial variations [12, 13] than those from the M2 continuous laser. These samples were fabricated utilizing the following parameters: Laser power 200 W; Layer spacing 50 µm; Hatch Spacing 100 µm; Beam Diameter of 0.070 mm; Point Spacing of 60 µm; Exposure time of 80 µs; with a melt strategy of meander. These samples were then subjected to post-process HIP treatment.

**Table 3. Heat Treatment Parameters.**

| Temperature | 1100 ℃ HIP | 1100 ℃ | 650 ℃ |
|---|---|---|---|
| Time | 60 mins | 60 mins | 30 mins |
| Pressure | 100 MPa | 0 MPa | 0 MPa |
| Quench | Group 1 | Group 2 | Group 4 |
| Furnace Cool (10 ℃/min) | - | Group 3 | Group 5 |
| Group 1 | L1-01, L1-02, L1-03, L1-04<br>L2-01, L2-02, L2-03, L2-04 | | |
| Group 2 | L1-05, L1-06, L1-07, L1-08<br>L2-05, L2-06, L2-07, L2-08 | | |
| Group 3 | L1-09, L1-10, L1-11, L1-12<br>L2-09, L2-10, L2-11, L2-12 | | |
| Group 4 | L1-13, L1-14, L1-15, L1-16<br>L2-13, L2-14, L2-15, L2-16 | | |
| Group 5 | L1-17, L1-18, L1-19, L1-20<br>L2-17, L2-18, L2-19, L2-20 | | |

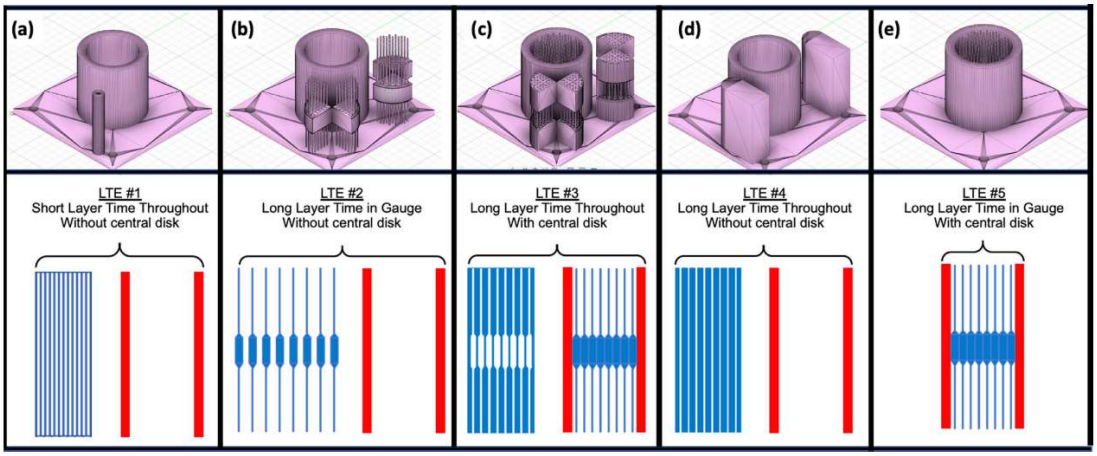


**Figure 7: 3D and schematic overview of the cylindrical geometries (a, b, c, d, and e) designed to modify the layer time as a function of cylinder height utilized in the LTE build [13].**

Laser power and velocities are generally constant during most L – PBF builds. The result of this consistency is that the scanning time spent of the laser for a given cross-section of the build at a given height is directionally proportional to the area of that particular cross-section. This concept may be referred to as a "layer – time" for each individual section of an additively manufactured build. These samples were built to evaluate the role of this layer time on defect formation, microstructure evolution and their cumulative role on the overall tensile properties. It was confirmed that these heterogeneities can be minimized by employing hot isostatic pressing (HIP) with subsequent solution anneal heat treatment. These samples were then compared to the other samples in this study to investigate the presence or lack of nanoscale partitioning and were also included in the X – ray diffraction analysis.

### *2.1.4 Porosity Study*

The fourth sample set was also built on the Renishaw SLM printer at the MDF and will be referred to as the porosity build. This sample set was initially fabricated as a part of an EPRI & DOE project studying the effect of porosity, whether HIP/SA heat treatments could close such pores, and the effect of this on the mechanical properties. These samples contained varying sizes of engineered pores (200 μm, 350 μm, and 500 μm) and varying percent volumes (1%, 3%, and 5%) of engineered pores. The results of this experiment have been previously published and were discussed in the literature review section [13].
To summarize here, HIP/SA was found to be sufficient to minimize any scatter of AM 316L stainless steel components for use in nuclear applications. This further confirmed AM 316L components as being able to meet and, in some cases, exceed industry and regulatory standards; further suggesting the ability for immediate deployment of AM components in nuclear applications without the need of post heat treatments. These samples were also included in the X – ray diffraction analysis.

## 2.2 Characterization

### *2.2.1 Optical Microscopy*

Optical microscopy images were obtained on the Zeiss Axio at the Manufacturing Demonstration Facility (MDF). Samples from the parameter study and samples 0329, 0330, 0331, and 0332 of the LTE sample set were electrolytically etched using 10g oxalic acid dissolved in 100ml distilled water at 50-60 mA for 6

minutes. These samples were examined optically after etching. Etched optical images were instrumental in the initiating the current investigation into stark etching contrast. They also led to further etched EBSD for selecting regions of interest for STEM/EDS analysis and for automated segmentation with Emerald; both of which will be discussed later.

### *2.2.2 EBSD*

All electron backscatter diffraction data was acquired on the Zeiss EVO SEM at the MDF. Electron backscatter diffraction was used to investigate samples from the Parameter Study samples, the LTE samples, and the Porosity Study samples. All SEM and EBSD images were acquired at 20 kV, 5000 pA, and with a working distance of approximately 15–20 mm. EBSD images were subsequently analyzed with TEAM™ EDS Software Suite. All images had a store resolution of 1024 × 800 matrix and 2 × 2 binning.

### *2.2.3 STEM/EDS*

Scanning transmission electron microscopy (STEM) and energy dispersion x – ray spectroscopy (EDS) data were obtained on the Talos at Oak Ridge National Laboratory (ORNL) at 30 kV by Dr. Donovan Leonard. STEM/EDS was used to investigate sample 6 from the Parameter Study samples and sample 0331 from the LTE samples. Three regions of interest were selected from sample 6 of the parameter study, Figure 8 (a). Focused Ion Beam (FIB) was used to remove site specific lift – outs, Figure 8 (b), performed with the Hitachi NB5000 FIB/SEM at the MDF. Specific areas, across an entire weld pool, were targeted for lift – out so that solidification structures from the edge weld pool to the center of the weld pool could be investigated. The FIB lift – out starts with deposition of a ∼500 nm thick layer of W onto the cross – section surface using ion beam deposition. This W layer is placed in order to reduce any “curtaining” effect during the final FIB milling of the specimen. The milling of the region of interest started with a 40 kV, 3.36 nA beam. The beam current was then reduced to 0.52 nA, and the sample was further thinned to electron transparency.

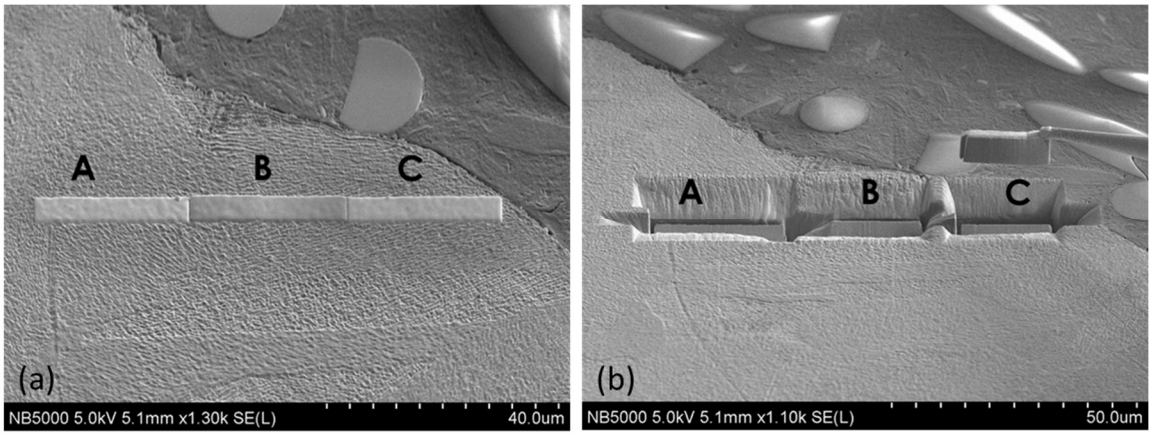


**Figure 8: Sample 6 of the parameter study region of interest (a) before and (b) after FIB.**

Scanning transmission electron microscopy (STEM) high-angle annular dark field (HAADF) and bright field micrographs were collected using the FEI Talos F200X, which was equipped with a symmetric A-TWIN objective lens integrated with the SuperX energy-dispersive spectrometer (EDS) system and operated at 200kV. The silicon drift detector SuperX system gives the Talos a solid angle of 0.9 mrad, thereby maximizing the collection efficiency during x-ray analysis and mapping.

Quantification line scans of EDS maps was performed using the Quantax Esprit 3.0 software with Cliff – Lorimer approximation on the Optimus/Quantax PC at the MDF.

### *2.2.4 XRD*

X – ray diffraction (XRD) data was acquired at the Joint Institute for Advanced Materials (JIAM) on the Malvern Panalytic Diffractometer. XRD data was acquired for all samples in all builds studied using the data collection parameters found in Table 4. Additionally, both 5 mm and 10 mm masks were used as the samples were neither uniform in size nor placement within the mounts. The resultant area of each sample included for data collection for all sample sets may be found in Table 5.

All refinements were performed with HighScore Plus version 4.7 software package. A Silicon parameter file was utilized to negate any peak broadening attributed to the instrument. Rietveld and strain refinements were performed on all samples from all four builds. Refinement parameters are listed in Table 6.

**Table 4: Scan Parameters for X – Ray Diffraction Data Collection**

| | |
|---|---|
| **Instrument Parameters:** | |
| Instrument Used | Malvern PANalytical Diffractometer |
| Stage Used | Reflection-Transmission Spinner |
| Detector Used | PIXcel 3D Scanning Mode |
| *Collimation (Incident)* | |
| Divergence Slit [°] | 0.25 |
| Anti-scatter Slit [°] | 0.25 |
| Goniometer Radius [mm] | 240 |
| Beam Type | Co $K_{\alpha 1}$ to $K_{\alpha 2}$ |
| **Data Collection Parameters:** | |
| Software Package | HighScore Plus v4.7 |
| Temperature [℃] | 25 |
| Pressure | Ambient |
| Operating Voltage [kV] | 45 |
| Operating Current [mA] | 40 |
| *Goniometer Parameters* | |
| Wavelength [Å] | 1.79 |
| Scan Range [° 2θ] | 45.0 < 2θ < 130.0 |
| Step Size [° 2θ] | 0.013 |
| Scan Step Time [s] | 23.970 |

**Table 5: Table of Masks and Area for all Samples Studied.**

| Mask | 5mm | 10mm |
|---|---|---|
| Area | 2.74mm x 7mm | 2.74mm x 12mm |
| Parameter Study Samples | 5, 9, 11, 14, 19, 23, 24, 25, 26, 27, 28, 29 | 1, 2, 3, 4, 6, 7, 8, 10, 12, 13, 15, 16, 17, 18, 20, 21, 22 |
| Tensile Heat Treatment Study Samples | L1-01, L2-01, L2-05, L2-17, L1-26, L2-26 | L1-05, L1-09, L2-09, L1-13, L2-13, L1-17 |
| LTE Study Samples | - | ALL |
| Porosity Study Samples | Con HIP xz, Con NoHIP xz | Con HIP xy, Con NoHIP xy |

**Table 6: Refinement Parameters by Refinement Type.**

| | Reitveld Refinement | Strain Refinement |
|---|---|---|
| Global | Specimen Displacement<br>Background | Specimen Displacement<br>Background |
| Phase Dependent | Scale Factor<br>March-Dollase Factor<br>Lattice Parameter, a<br>U<br>W<br>Peak Shape 1<br>Peak shape 2 | Scale Factor<br>March-Dollase Factor<br>Lattice Parameter, a<br>U<br>W<br>Peak shape 1<br>Peak shape 2 |

# CHAPTER 3 RESULTS AND DISCUSSION

## 3.1 Experimental Analysis

Stainless steel, in particular 316L, was selected for this study because it is typically chosen for nuclear applications as it is an austenitic stainless steel and is advantageous due to its corrosion resistance, strength, and ductility.
A multi – length scale, from mm to nm, characterization methodology [18] was utilized in order to understand the spatial heterogeneity of the microstructures of these L – PBF additively manufactured components, and to understand the physical phenomena at different length scales. It has been shown that spatial variation of thermal cycles could lead to significant variations in primary dendrite arm spacing, ~0.7 – 3.5 μm [12]. This is predominant in regions with a lower thermal mass, which then leads to a slow cooling rate when processing conditions are held constant. Slower cooling rates lead to slow melt pool solidification rates resulting in coarser primary dendrite arm spacing, as well as potentially playing a role in the phase selection ($\delta$-ferrite (BCC) phase or $\gamma$-austenite (FCC) phase) phenomena [19, 20]. Therefore, select samples that were believed to have a tendency to cool at different rates were selected for further analysis. This multi – length scale investigation will include optical microscopy, EBSD, XRD, and STEM/EDS; as well as theoretical modeling with the Interface Response Function (IRF), the Semi – Analytical Heat Transfer Model (SAHTM), and thermodynamic modelling with Thermocalc. All of this will be discussed in turn.

## 3.2 Early Hypothesis

### *3.2.1 Rationalization*

As discussed previously, the etched optical micrograph of sample 6 from the parameter study shown in Figure 9 (a) reveals an interesting and stark contrast distribution. The grains near the edge of the melt pool region appear dark, while grains toward the center of the melt pool region appear bright. Thus, a brief initial hypothesis was developed that these etching contrasts could be due to changes in crystallographic orientations. However, preliminary EBSD data, as seen in Figure 9 (c), indicated that there was no clear one – to – one correlation between this etching contrast and crystallographic orientations. Therefore, based on

welding metallurgy theories [16, 17, 18, 20] an early hypothesis was developed that this unique etching contrast could be due to the presence of fine remnant δ-ferrite (BCC) structure dispersed within γ-austenite (FCC) dictated by the solidification path. This early hypothesis is also based on the etched optical micrographs being >50% lightly etched combined with the fact that the sample is 316L which is an austenitic stainless steel meaning that the greater portion, whether lightly or darkly etched, can be expected to be γ-austenite (FCC).

The different solidification paths that are possible for stainless steels that are observed to be fully austenitic are of significant importance in this study and must be fully considered, as shown in Figure 10. Upon cooling from liquid there are four possible paths as has previously been touched on in the background section. Two of these solidification paths are dendritic growth and two are planar growth. The AM parameters investigated in this study produce high thermal gradients (G) and high solidification rates (R ~ $10^4$ K/s), Figure 11. High G in conjunction with high R leads to cellular dendritic growth. The four solidification paths are as follows: 1 – dendritic δ - ferrite (BCC) solidification, Figure 10 (a), where Ni partitioning will be found in the inter – dendritic regions. Ni is an austenite stabilizer and will move out of the δ - ferrite (BCC) into the inter – dendritic regions. as it solidifies. 2 – Planar δ - ferrite (BCC) solidification, which is not expected here, Figure 10 (b). 3 – Dendritic γ-austenite (FCC) solidification, Figure 10 (c), where Cr & Mo partitioning will be seen in the inter – dendritic regions as they are both ferrite stabilizers and both will move out of the γ-austenite (FCC) into the inter – dendritic regions. 4 – Planar γ-austenite (FCC) solidification, which is not expected here, Figure 10 (d).

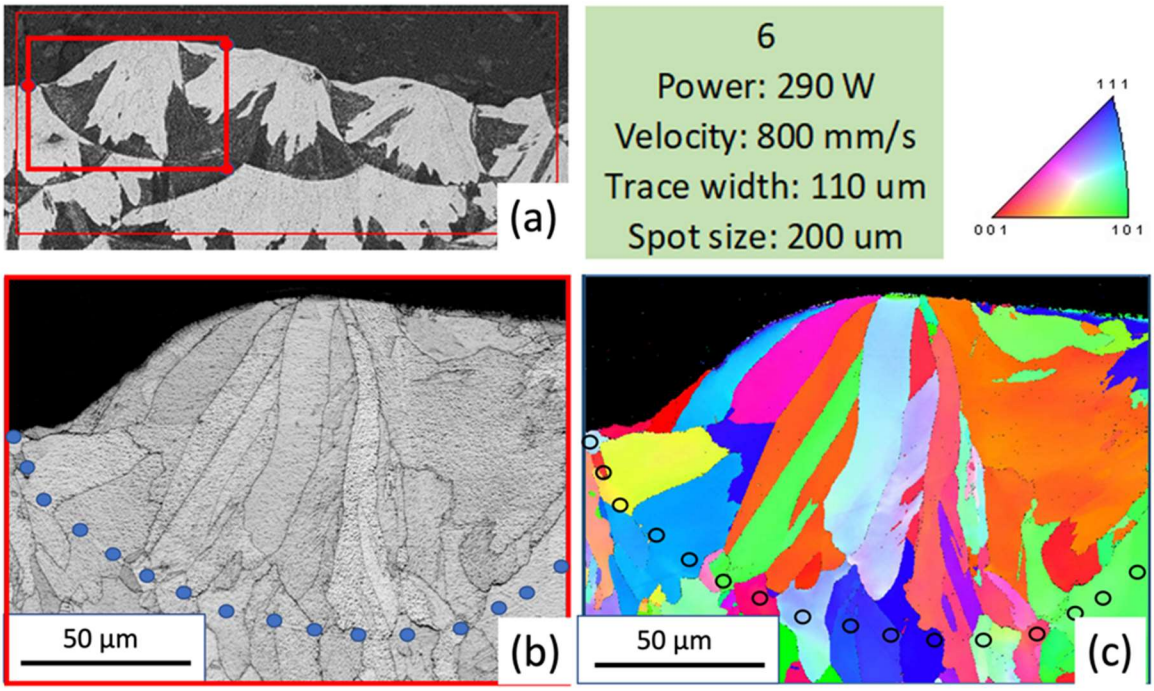


**Figure 9: (a) Etched optical image of the region near the top of the build from sample 6 showing darkly and brightly imaging regions; (b) SEM; and (c) EBSD) imaging from the red box region from (a). Ref: Unpublished research by Simpson and Leonard et al.**

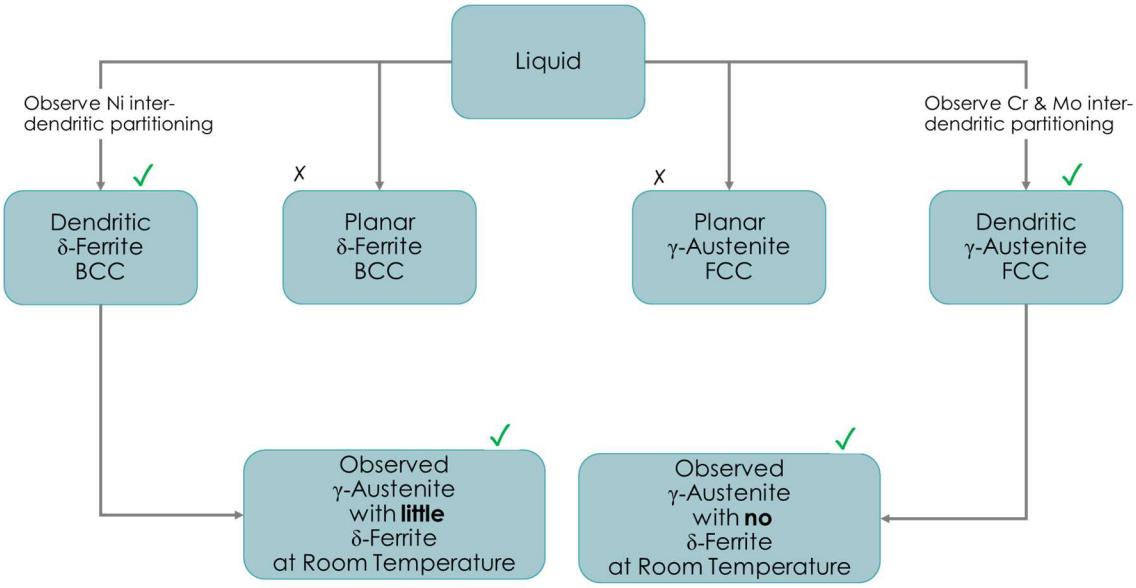


**Figure 10: Potential solidification pathways; (a) dendritic δ - ferrite (BCC) with Ni partitioning to inter – dendritic regions, (b) planar δ - ferrite (BCC), (c) dendritic γ - austenite (FCC) with Cr & Mo partitioning to inter – dendritic regions, and (d) planar γ - austenite (FCC).**

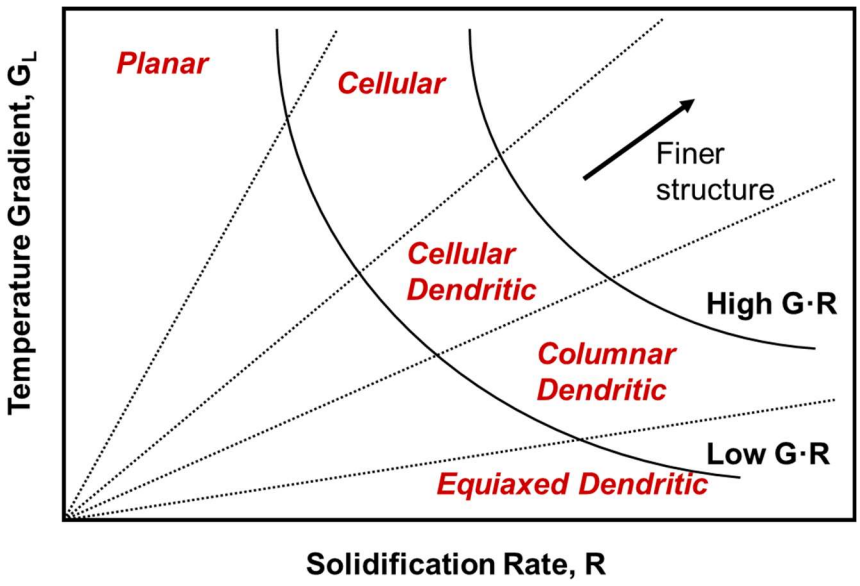


**Figure 11: Thermal Gradient (G) and Solidification Rate (R) solidification determination chart under normal welding conditions.**

### *3.2.2 Findings*

The early hypothesis of the etching contrast led to comprehensive scanning transmission electron microscopy (STEM) analysis of sample 6 of the parameter study with concurrent energy dispersive x – ray spectroscopy (EDS) analysis [21]. The etched optical and EBSD images, Figure 12, were used to select a region of interest for STEM/EDS analyses. STEM/EDS data was collected from three regions from location A, Figure 13 (a). An EDS map from region 2A1, Figure 13(b), of location A, representing the darkly etched region located at the edge of the weld pool revealed Cr & Mo inter – dendritic partitioning, Figure 14, suggesting dendritic $\gamma$-austenite (FCC) solidification. These findings were exactly opposite of the solidification and partitioning patterns expected in the early hypothesis. Again, the early hypothesis expected the darkly etched regions to reveal dendritic $\delta$ - ferrite (BCC) solidification. This resulted in a revised hypothesis informed from these initial STEM/EDS results, theoretical IRF modeling, theoretical SAHTM modeling, and thermodynamic modeling.

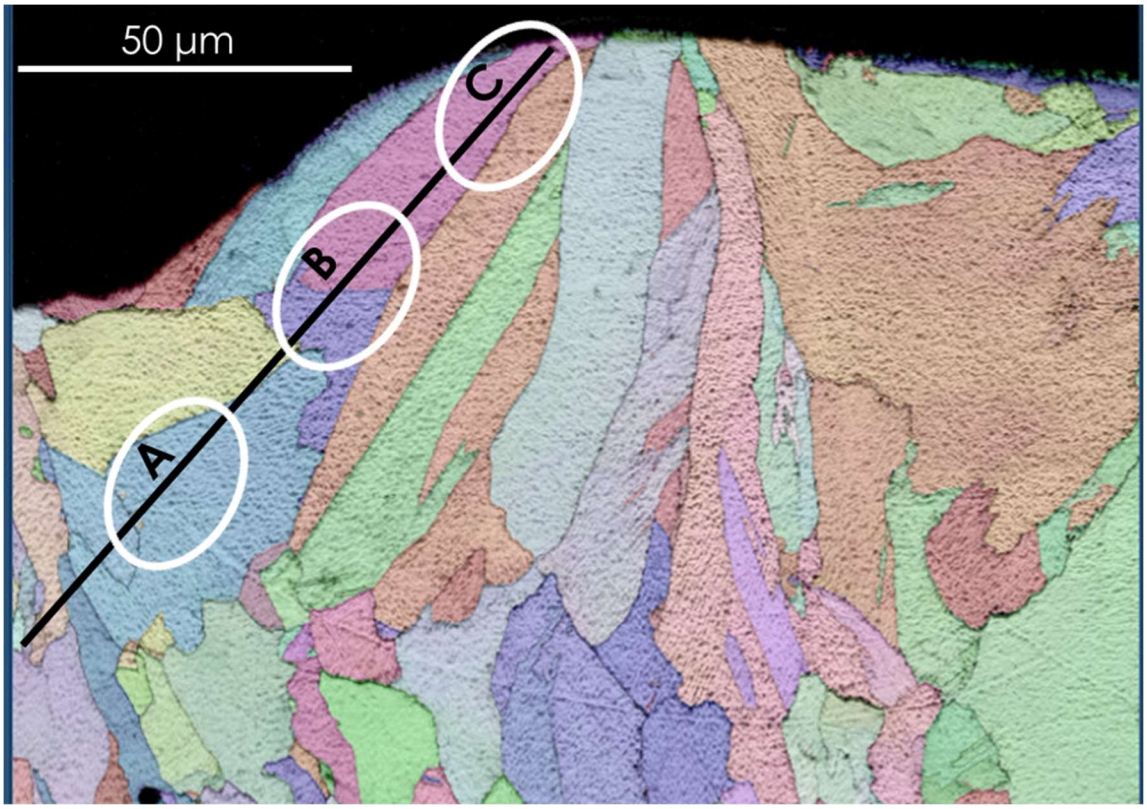


**Figure 12: EBSD image with three regions of interest selected. Region A contains the edge of the weld pool that etched darkly, region B contains the transition of dark to light etching, and region C contains the center of the weld pool that etch lightly. Ref: Unpublished research by Leonard et al.**

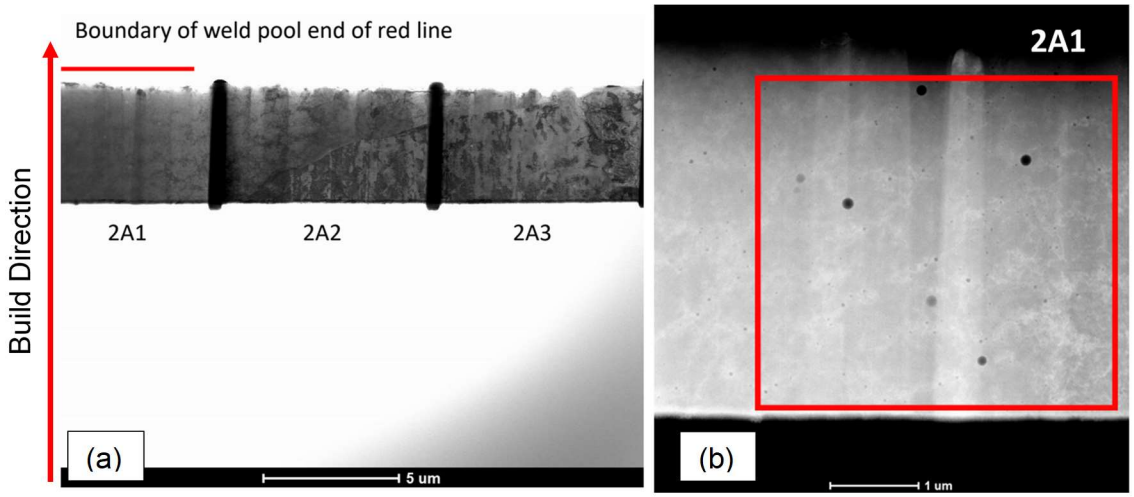


**Figure 13: Location A of sample 6 from the parameter study build, (a) Bright Field (BF) image of all three regions of location A, and (b) High-angle annular dark-field (HAADF) image of EDS map area of region 2A1. Ref: Unpublished research by Leonard et al.**

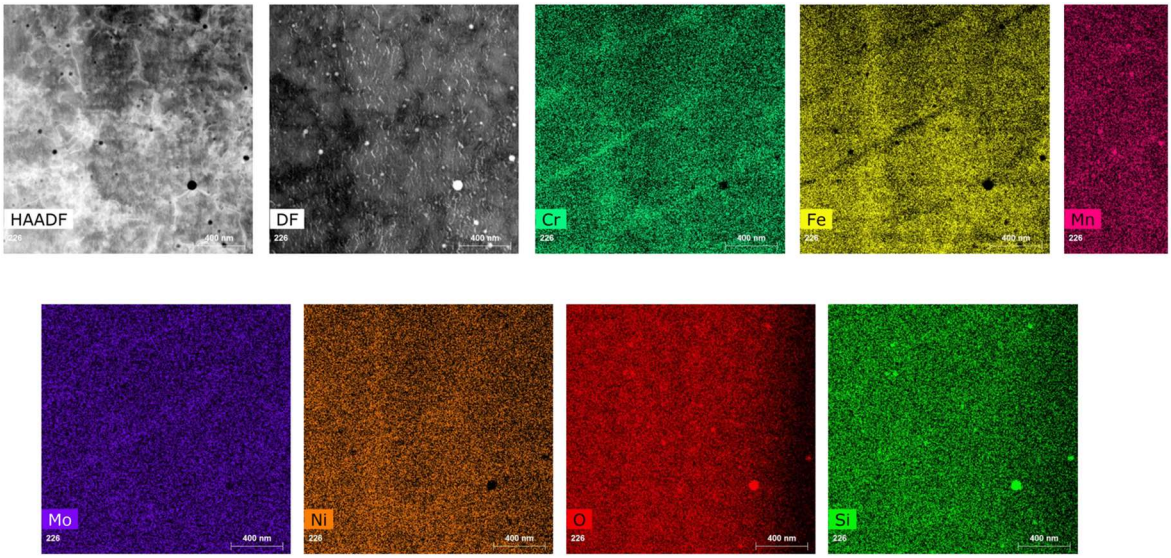


**Figure 14: Unquantified EDS map of region 2A1 of location A showing clear Cr & Mo partitioning. Ref: Unpublished research by Leonard et al.**

## 3.3 Revised Hypothesis

The unquantified EDS maps of location A revealed Cr & Mo inter – dendritic partitioning indicating initial solidification as $\gamma$-austenite (FCC), which was directly opposite of the solidification path and partitioning patterns expected with the early hypothesis. These findings illustrated a need for a revised hypothesis.

### *3.3.1 Rationalization*

To form a revised hypothesis required a return to the metaphorical drawing board. The revised hypothesis will be based first on the initial STEM/EDS findings. If the darkly etched region revealed Cr & Mo partitioning indicating $\gamma$-austenite (FCC) solidification, then will the lightly etched region reveal Ni partitioning? Theoretical and thermodynamic modelling will also be leveraged to inform the revised hypothesis.

### *3.3.2 Theoretical Modeling – IRF*

The theoretical calculations based on Interface Response Function (IRF) theories [17, 22] were performed to predict the primary solidification phase as a function of the maximum solidification velocity for sample 6 of the parameter sample study as there are limitations associated with the complexity to characterize the high-temperature $\delta$-ferrite (BCC) phase.

The IRF was utilized to predict the primary solidification phase as a function of solidification velocity, using the initial composition found in Table 7. The IRF code was initially developed by Babu et. al. (Appendix A) with modifications made to perform a sensitivity analyses for phase selection calculations. First, calculations were performed using the default values used by Galicki et al [14], then by calibrating the diffusion coefficient of BCC ($D_\alpha$) from $10^{-9}$ to $10^{-8}$ $m^2/s$; as shown in Figure 15. This calibration reveals the ability of $\gamma$-austenite (FCC) to form at low speeds and the $\delta$ - ferrite (BCC) to form at high speeds, as seen in Figure 15 (b).

The calibrated IRF model predicts dendritic γ-austenite (FCC) solidification giving way to dendritic δ - ferrite (BCC) solidification at approximately $10^{-1}$ m/s, Figure 16 (a). Again, planar growth was not plotted as it is not expected at the high cooling rates found in this study of $10^4$ K/s. The IRF prediction of solidification beginning with dendritic γ-austenite (FCC) is in agreement with the observed unquantified EDS results from location A at the weld pool edge. Additionally, Figure 16 (b), illustrates expected solidification paths predicted for the complete range of solidification velocities of all parameter study samples, labeled G&R (Concept) in the figure. The G&R (Concept) label refers to the G&R values calculated with the IRF for all parameter study samples which were fabricated on the M2 Concept laser system.

### *3.3.3 Thermodynamic Modeling – Thermocalc Scheil Solidification Models*

Thermocalc was used to provide clarity and evidence for both the partitioning patterns as well as the hypothesized solidification path. Scheil solidification models were calculated for both γ-austenite (FCC) and δ-ferrite (BCC) equilibrium solidification of the parameter study composition of 316L stainless steel. The γ-austenite (FCC) Scheil solidification model, seen in Figure 17, predicts the Cr and Mo enrichment that was found in the unquantified STEM/EDS analysis of the darkly etched region of location A. The δ-ferrite (BCC) Scheil solidification model, seen in Figure 18 predicts the Ni enrichment that is now hypothesized to be found in the STEM/EDS analysis of the lightly etched regions. These models lend further weight to the unquantified STEM/EDS findings of location A and the revised hypothesis of initial solidification as γ-austenite (FCC) in the darkly etched regions and δ-ferrite (BCC) in the lightly etched regions.

**Table 7. Composition of All Four Builds.**

| Element | | C | Co | Cu | Cr | Fe | Mn | Mo | N | Ni | O | P | S | Si |
|---|---|---|---|---|---|---|---|---|---|---|---|---|---|---|
| Parameter Study Build | wt% | 0.001 | 0.08 | 0.00 | 16.81 | 67.3 | 0.99 | 2.43 | 0.01 | 11.92 | 0.05 | 0.005 | 0.00 | 0.36 |
| Tensile Study Build | wt% | 0.006 | 0.10 | 0.01 | 17.07 | 66.6 | 1.19 | 2.41 | 0.01 | 12.08 | 0.05 | 0.005 | 0.00 | 0.46 |
| LTE Study Build | wt% | 0.014 | 0.00 | 0.052 | 17.69 | 65.5 | 1.31 | 2.37 | 0.084 | 12.35 | 0.03 | 0.015 | 0.004 | 0.56 |
| Porosity Study Build | wt% | 0.014 | 0.00 | 0.052 | 17.69 | 65.5 | 1.31 | 2.37 | 0.084 | 12.35 | 0.03 | 0.015 | 0.004 | 0.56 |

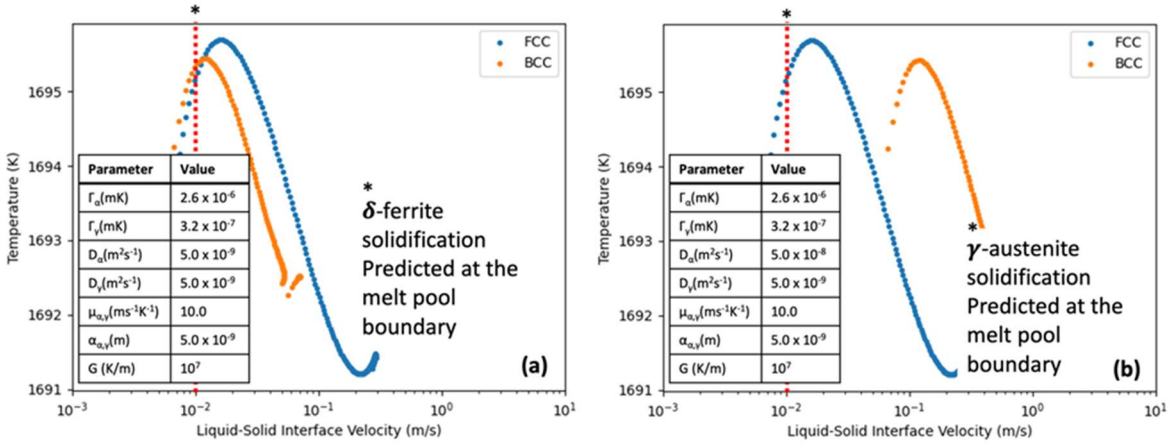


**Figure 15: IRF – sensitivity analyses for phase selection calculations: (a) default values used by Galicki et al [14]; (b) Calibration of $D_\alpha$ from $10^{-9}$ to $10^{-8}$ $m^2/s$ allows the γ-austenite to form at low speeds and the δ-ferrite to form at high speeds.**

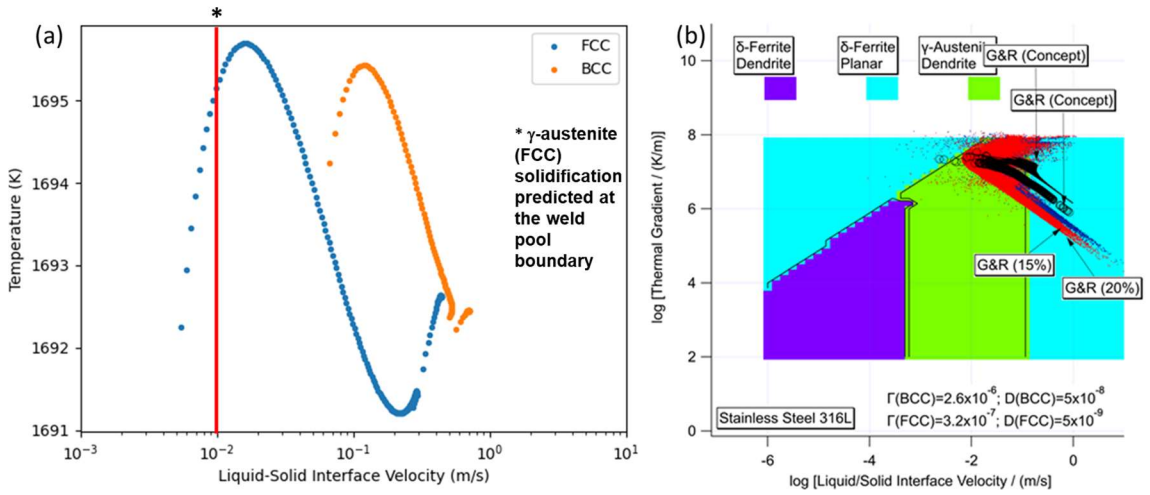


**Figure 16: (a) IRF plot of Temperature vs Liquid-Solid Interface Velocity of the maximum solidification velocity for sample 6 of the parameter study and (b) a log-log plot of Temperature vs Liquid-Solid Interface Velocity of the range of solidification velocities found in the porosity build demarcated by G&R (15%) and G&R (20%) labels; and the parameter study samples demarcated by the G&R (Concept) labels [13].**

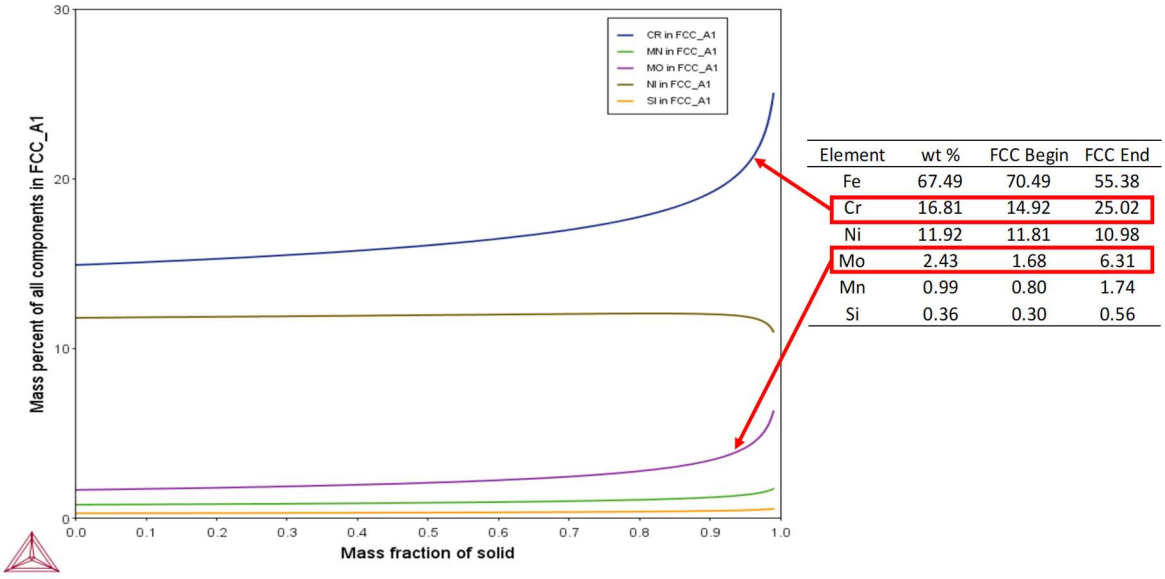


| Element | wt % | FCC Begin | FCC End |
|---|---|---|---|
| Fe | 67.49 | 70.49 | 55.38 |
| Cr | 16.81 | 14.92 | 25.02 |
| Ni | 11.92 | 11.81 | 10.98 |
| Mo | 2.43 | 1.68 | 6.31 |
| Mn | 0.99 | 0.80 | 1.74 |
| Si | 0.36 | 0.30 | 0.56 |

**Figure 17: Scheil solidification model of elemental enrichment during γ-austenite (FCC) solidification.**

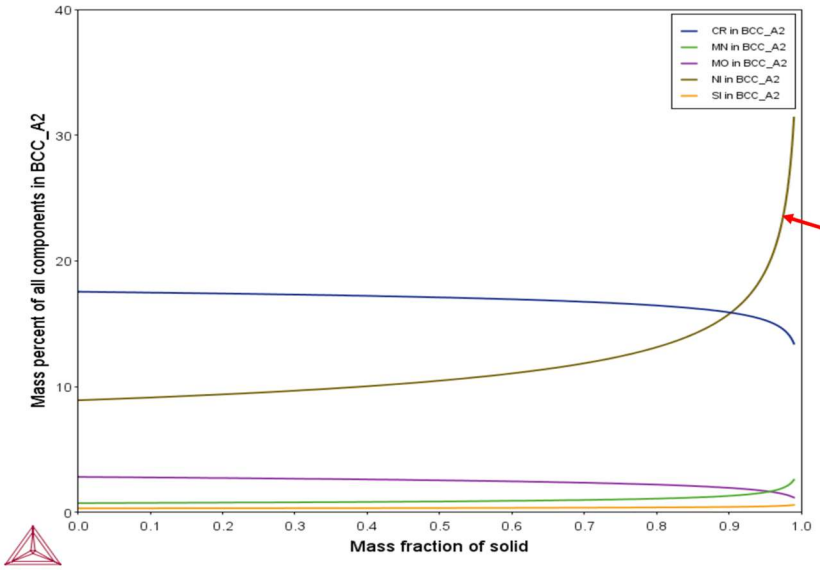


| Element | wt % | BCC Begin | BCC End |
|---|---|---|---|
| Fe | 67.49 | 69.70 | 50.84 |
| Cr | 16.81 | 17.54 | 13.41 |
| Ni | 11.92 | 8.91 | 31.41 |
| Mo | 2.43 | 2.81 | 1.17 |
| Mn | 0.99 | 0.73 | 2.59 |
| Si | 0.36 | 0.31 | 0.58 |

**Figure 18: Scheil solidification model of elemental enrichment during δ-ferrite (BCC) solidification.**

### *3.3.4 Findings – STEM/EDS*

Informed by both the theoretical models of the IRF and the Scheil solidification models, as well as the initial unquantified EDS results from location A, the revised hypothesis calls for initial solidification as $\gamma$-austenite (FCC) represented by the darkly etched regions and transitioning to $\delta$-ferrite (BCC) solidification represented by the lightly etched regions. To confirm this revised hypothesis EDS analyses were performed sequentially from location A to location C, beginning with quantification of the EDS results from location A. As previously mentioned, three regions from location A were imaged using High – Angle Annular Dark Field (HAADF) and Dark Field (DF) modes, as well as, characterized using EDS elemental mapping, as seen in Figure 19. Although only one region from location A is shown, all three regions from location A revealed clear Cr and Mo inter – dendritic partitioning. Further, a quantification line scan of the EDS maps of Figure 19 proved the validity of the Cr and Mo partitioning to the inter – dendritic regions, as seen in Figure 20. Although not shown, the maps confirmed that the melt pool regions contain Mn- and Si- rich nano – scale oxide inclusions as has been seen in other publications [5].

To further confirm the revised hypothesis STEM/EDS was performed on the remaining locations B and C. Interestingly, the partitioning pattern from the first left – hand region of location B, Figure 21(b) P2B1, that was located closer to location A showed similar partitioning patterns to those found in location A. That is region P2B1 of location B revealed Cr and Mo inter – dendritic partitioning in the unquantified EDS maps, Figure 22. However, this partitioning was not as “bright” as those seen in the EDS maps of location A. In the next step, the third right – hand region of location B that is closer to location C was analyzed, Figure 21(c) P2B3. The results reveal an interesting change in partitioning pattern as there was faint inter – dendritic Ni partitioning found, Figure 23.

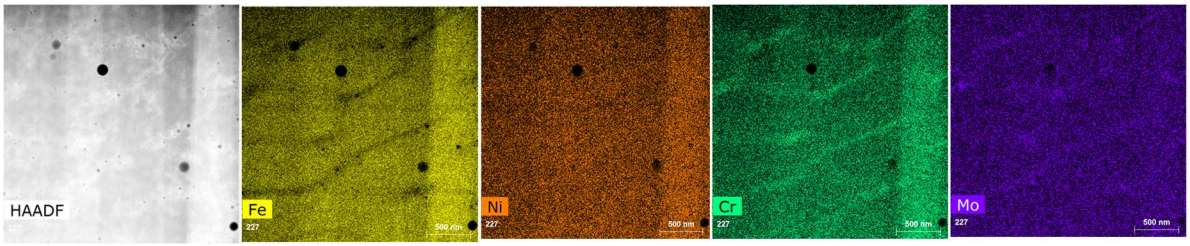


**Figure 19: HAADF image and EDS maps for parameter study sample 6, location A. Ref: Unpublished research by Leonard et al.**

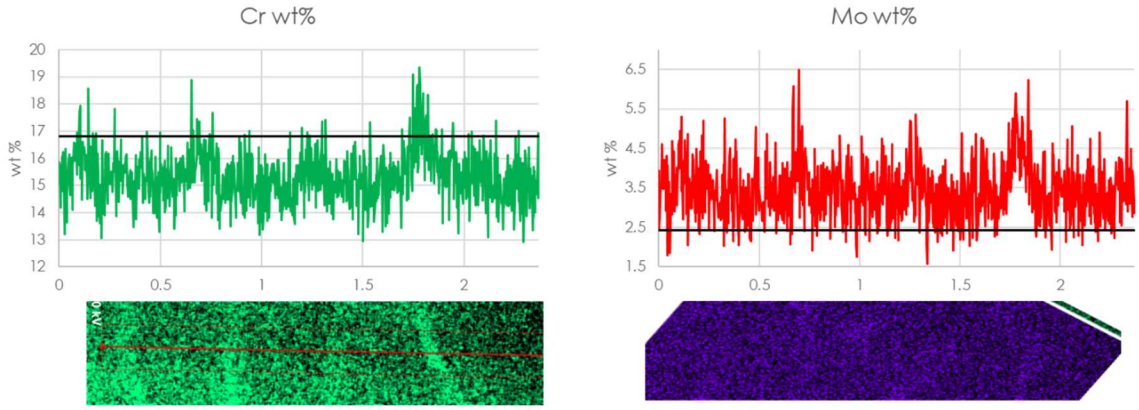


**Figure 20: Quantification line scan of parameter study sample 6 location A; confirming dendritic γ-austenite (FCC) solidification.**

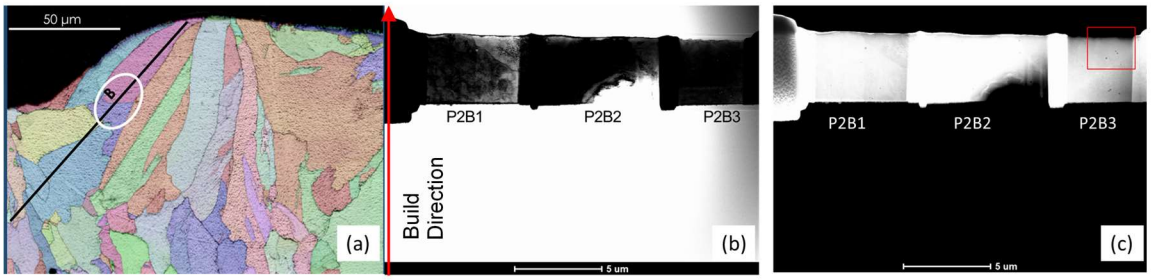


**Figure 21: Location B of the region of interest; (a) EBSD showing location B, (b) BF image of the 3 regions of location B selected for analysis, and (c) HAADF image of the three regions of location B with a red box around the region closer to location C. Ref: Unpublished research by Leonard et al.**

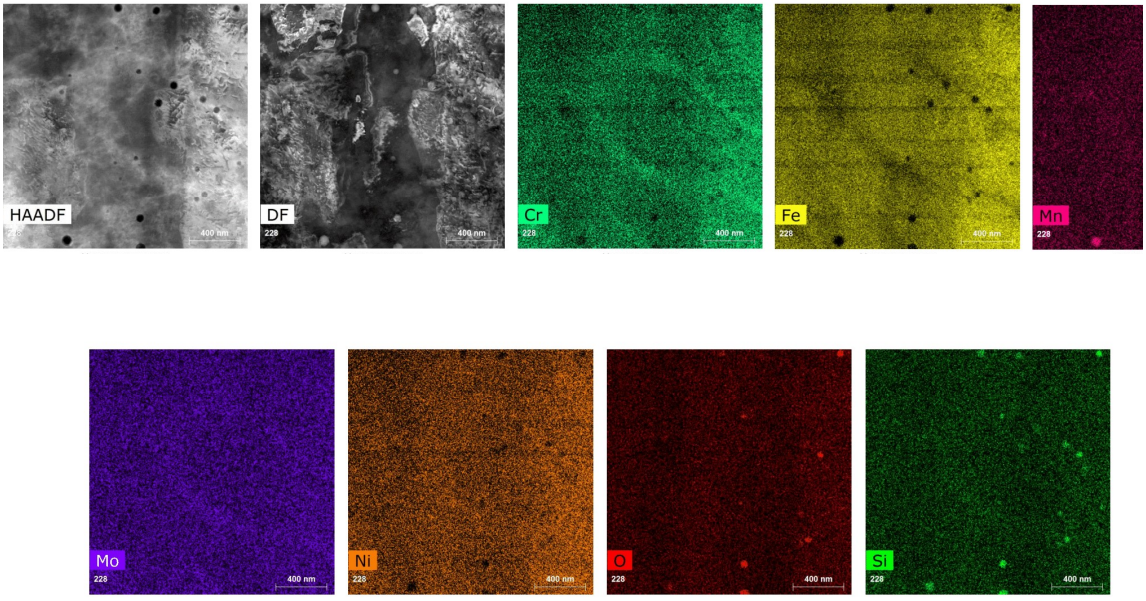


**Figure 22: HAADF image and EDS maps for parameter study sample 6 region B close to region A. Ref: Unpublished research by Leonard et al.**

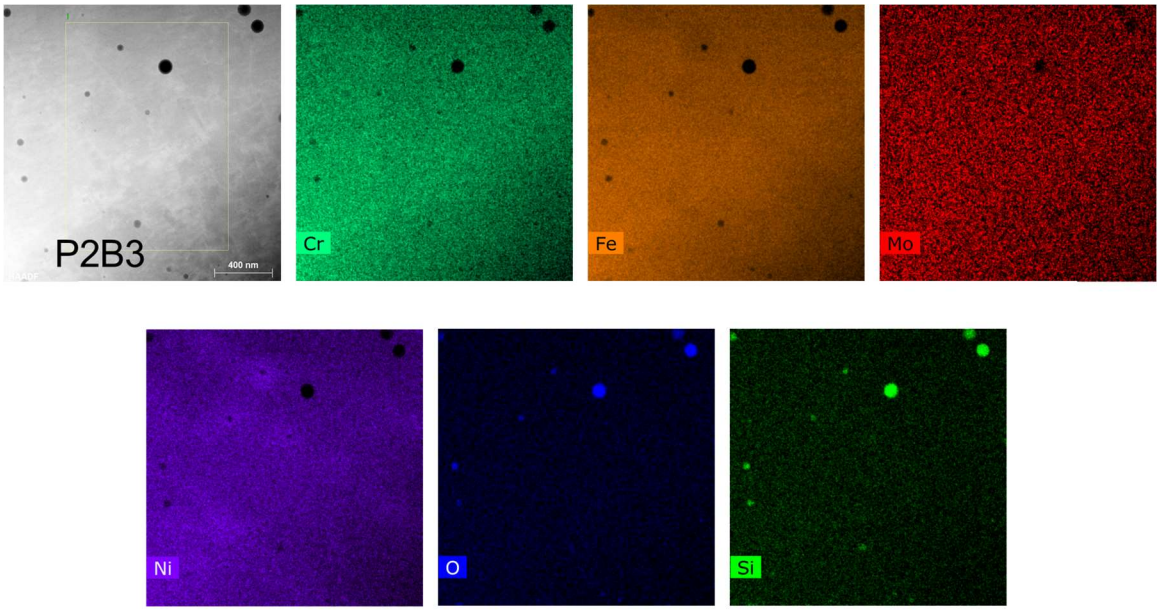


**Figure 23: HAADF image and EDS maps for parameter study sample 6 region B close to region C. Ref: Unpublished research by Leonard et al.**

Finally, location C was analyzed and inter – dendritic partitioning is expected according to the revised hypothesis. Location C did indeed reveal inter – dendritic Ni partitioning which was much more prominent in location C than in location B, Figure 24. Here Ni enriched regions are clearly associated with inter – dendritic boundaries. A quantification line scan of this EDS map proved the validity of the Ni partitioning to the inter – dendritic regions, as seen in Figure 25. Interestingly, the Mn-Si-O enriched inclusions were observed in all three regions of all three locations. Thus, the darkly etched regions were found to have undergone primary solidification of $\gamma$-austenite (FCC) phase with inter – dendritic partitioning of Cr and Mo, while the brightly etched regions were found to have undergone initial primary solidification of $\delta$-ferrite (BCC) with inter – dendritic partitioning of Ni, Figure 26. The initial solidification has now been determined, however, 316L stainless steels are known to be austenitic stainless steels suggesting a fully $\gamma$-austenite (FCC) room temperature phase structure. To determine the final resultant room temperature phase X – ray diffraction was performed to analyze all samples from all builds and the results will be discussed in the following section.

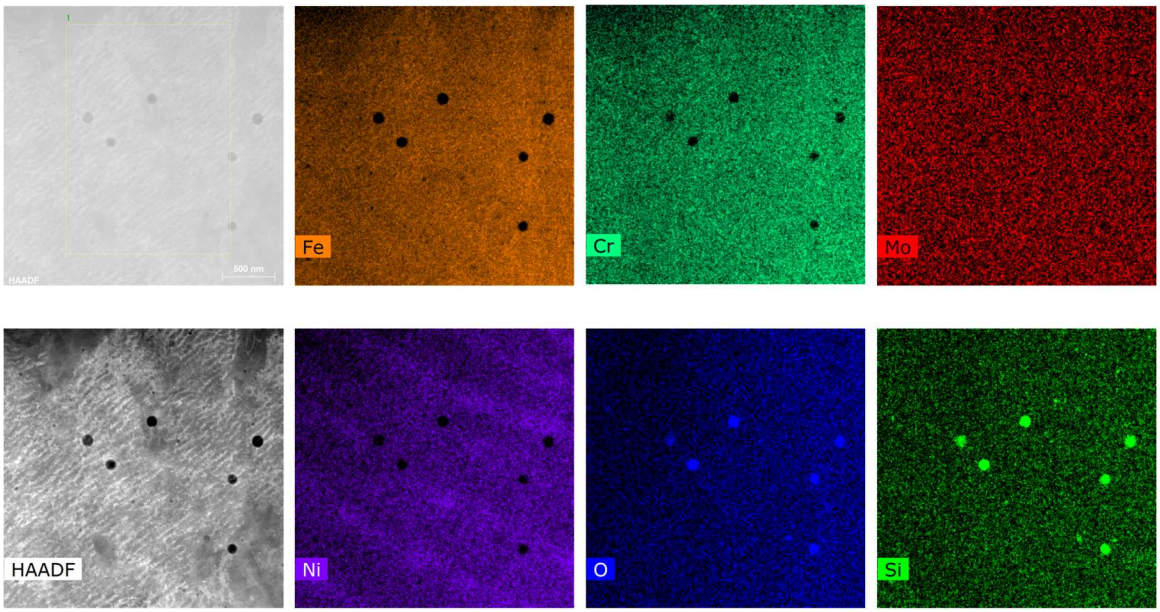


**Figure 24: HAADF image and EDS maps for parameter study sample 6, location C. Ref: Unpublished research by Leonard et al.**

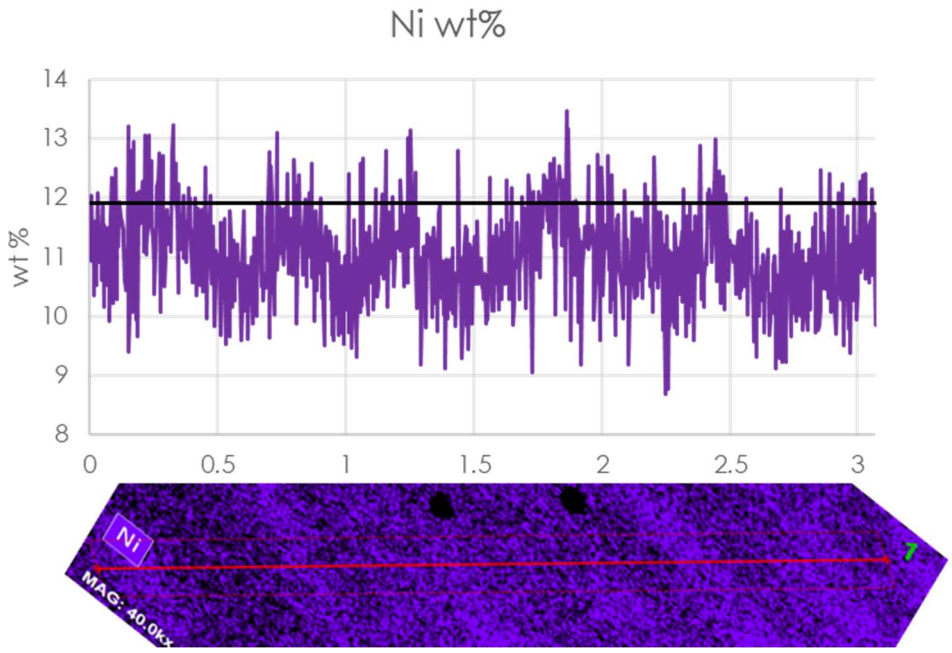


**Figure 25: Quantification line scan of parameter study sample 6, location C; confirming dendritic δ-ferrite (BCC) solidification.**

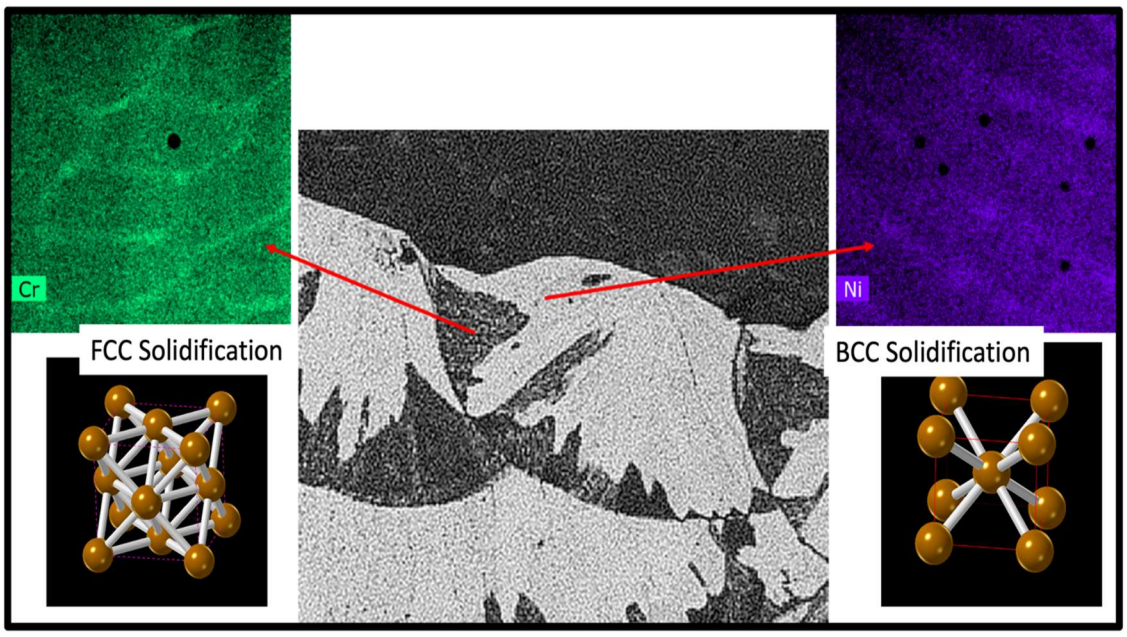


**Figure 26: Summary of initial solidification and subsequent elemental partitioning across weld pool.**

## 3.4 Final Observed Structure

### *3.4.1 XRD*

X – ray diffraction was employed to investigate whether the resultant room temperatures structure was a combination of $\gamma$-austenite (FCC) and $\delta$-ferrite (BCC), fully $\delta$-ferrite (BCC),or fully austenitic (FCC). All samples from all builds were characterized in this way. The XRD spectra for sample 6, Figure 27, shows 0.09 (4) % BCC. It is important to note that the small percentages of BCC found in all samples in this study are within the error of measurement and therefore may be the size/strain Rietveld refinements fitting to background noise.

The parameter study samples showed ≤ 0.50% $\delta$-ferrite (BCC) phase remaining in any samples of this build, as seen in Figure 28. The highest %BCC found in the parameter study was sample 11 with 0.50 % BCC. The tensile heat treatment study samples showed ≤ 1.0% $\delta$-ferrite (BCC) phase remaining in any samples of this build, as seen in Figure 29. The LTE Study samples showed ≤ 0.16% $\delta$-ferrite (BCC) phase remaining in any samples of this build, as seen in Figure 30. The porosity study samples showed ≤ 0.21% $\delta$-ferrite (BCC) phase remaining in any samples of this build, as seen in Figure 31. This investigation revealed that all samples irrespective of printer type, build parameters, and subsequent heat treatments were ≥ 99% $\gamma$-austenite (FCC). Based on the XRD results of ≥ 99% $\gamma$-austenite (FCC) final structure in conjunction with the quantified EDS evidence of remaining Ni partitioning from initial $\delta$-ferrite (BCC) solidification without any major diffusion before transformation to $\gamma$-austenite (FCC) it is believed that the solidification path found in the builds investigated is (a) liquid $\rightarrow$ $\delta$-ferrite $\rightarrow$ massive transformation to $\gamma$-austenite or (b) liquid $\rightarrow$ $\gamma$-austenite, Figure 32.

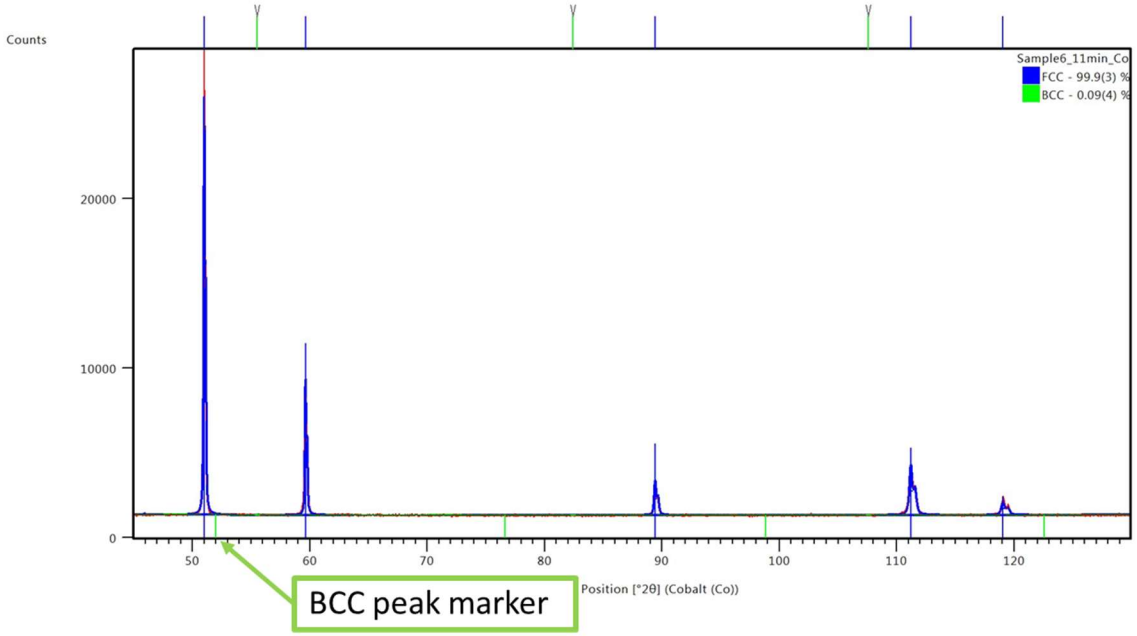


**Figure 27: XRD spectra for sample 6 of the parameter study.**

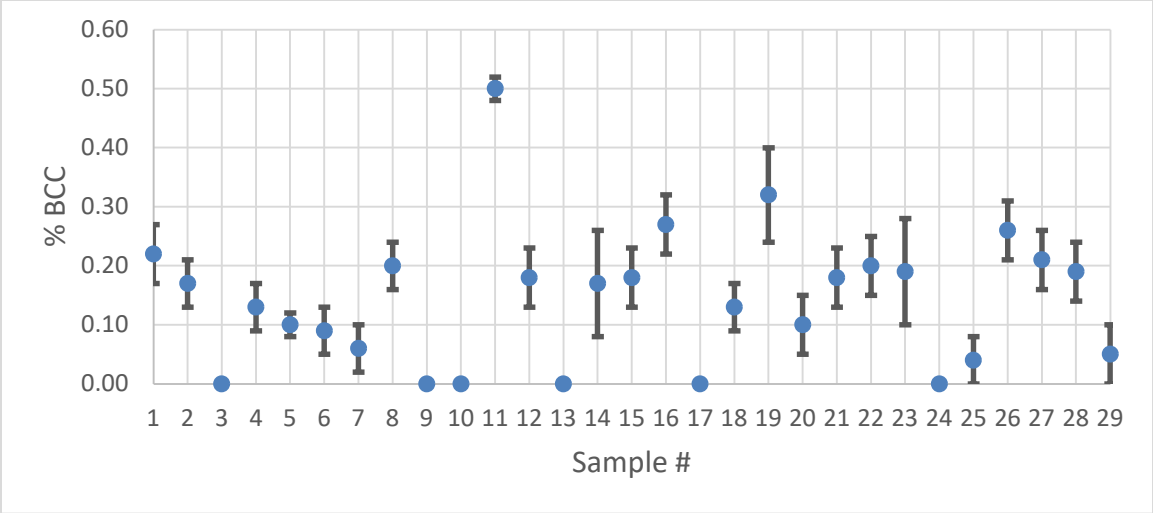


**Figure 28: X – ray diffraction results for the parameter study showing %BCC remaining.**

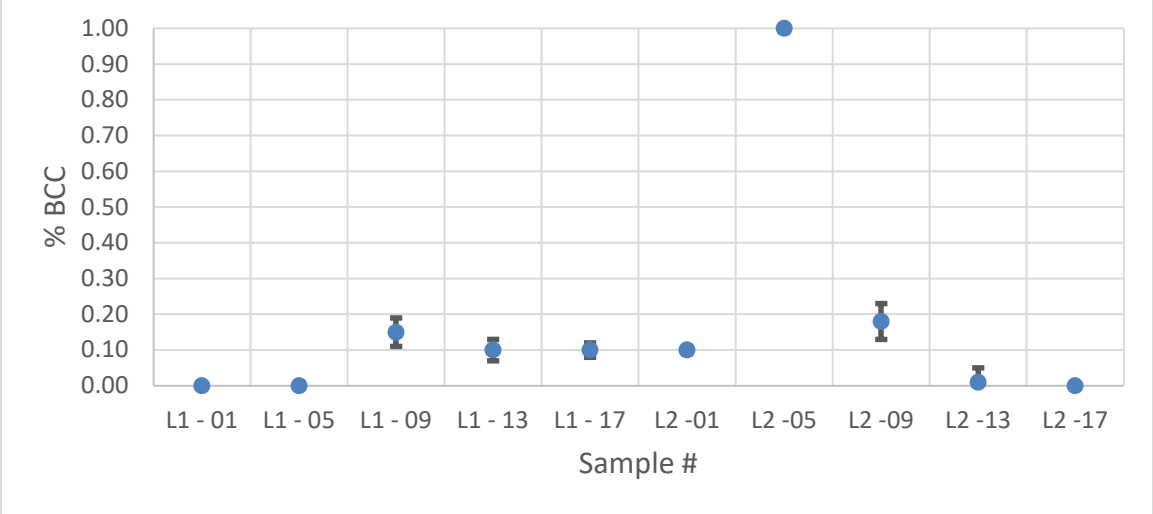


**Figure 29: X – ray diffraction results for the tensile heat treatment study showing %BCC remaining.**

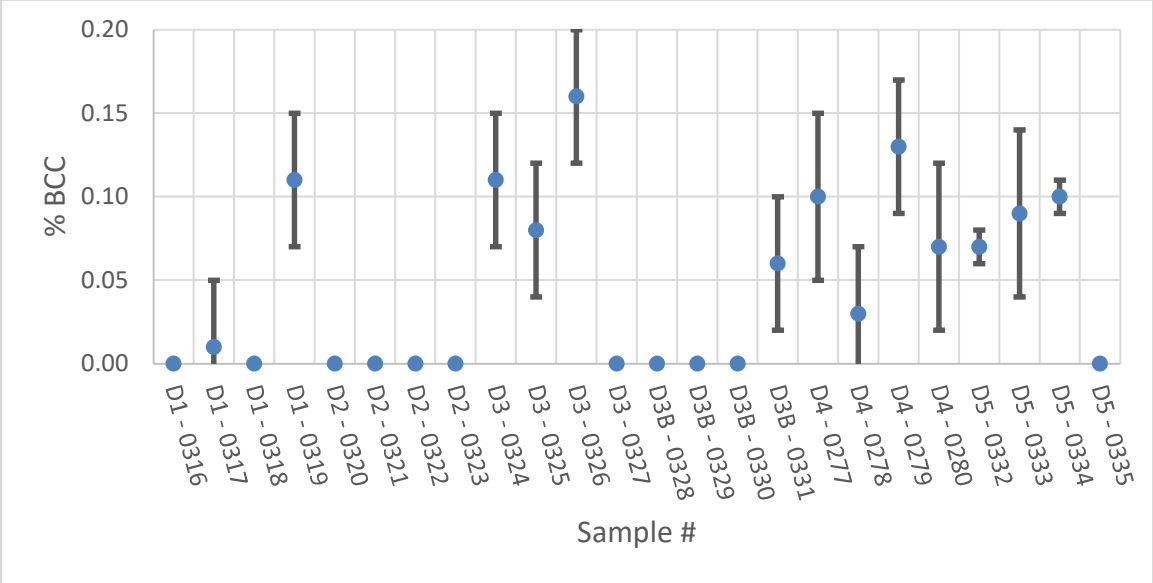


**Figure 30: X – ray diffraction results for the LTE study showing %BCC remaining.**

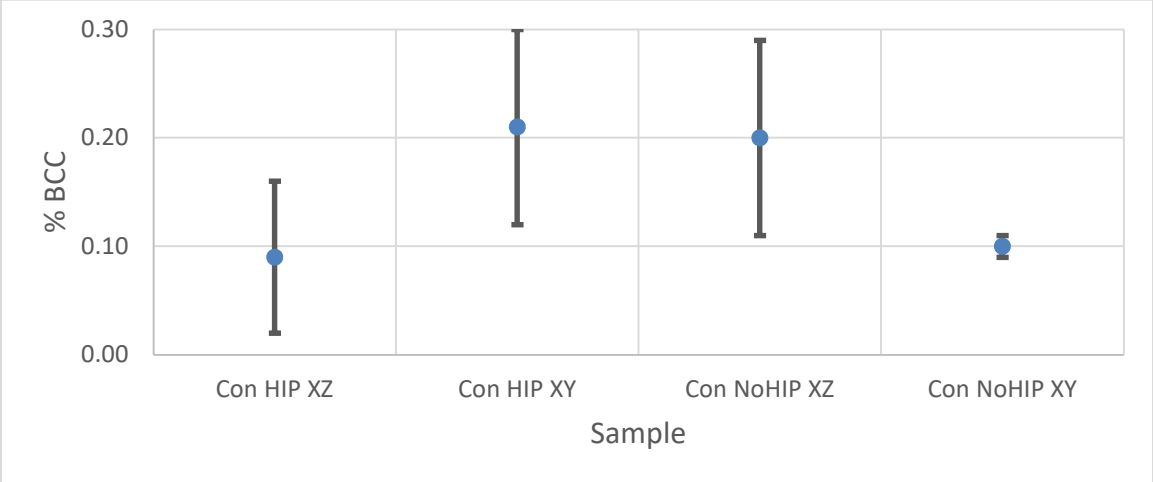


**Figure 31: X – ray diffraction results for the porosity study showing %BCC remaining.**

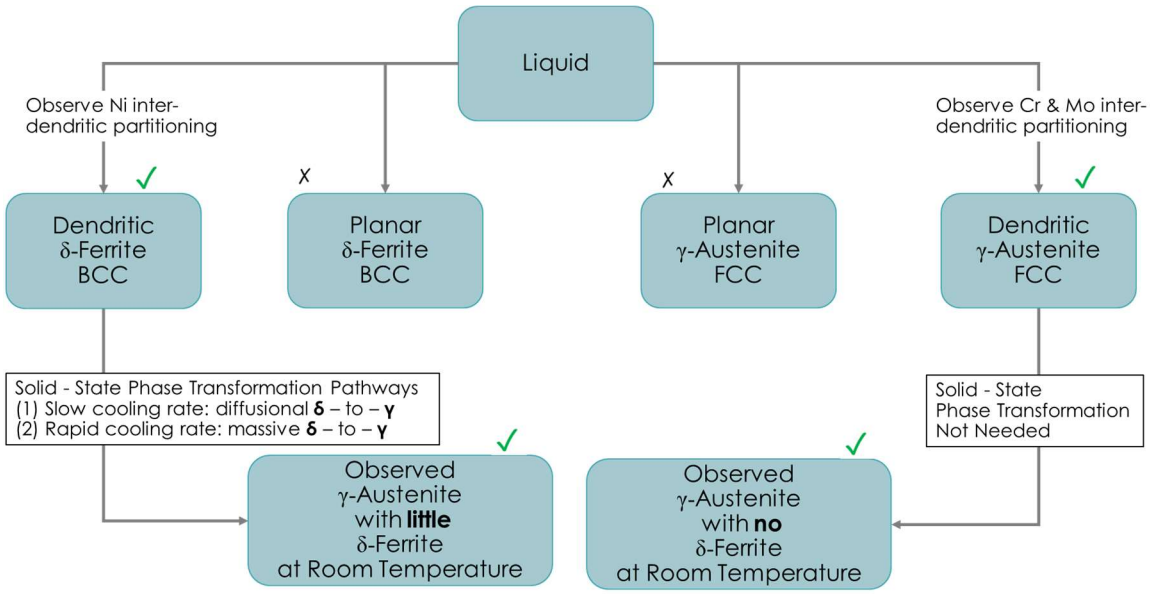


**Figure 32: Solidification pathways: (a) equilibrium: liquid → δ-ferrite → δ-ferrite + γ-austenite or (b) non-equilibrium: liquid → γ-austenite.**

As mentioned earlier, with the rapid cooling rates found in this study a massive transformation from δ-ferrite (BCC) to γ-austenite (FCC) is possible. This type of massive transformation would be “diffusionless” and would result in the Ni partitioning patterns remaining virtually untouched yet the room temperature resulting structure will have little BCC phase remaining. Such transformations can result in lattice strains which may be found through XRD as micro – strains.

The resulting percentages of micro – strain for each sample set is represented in Figure 33 – Figure 36. Interestingly, as could be expected, the samples in the as – fabricated status that did not undergo any heat treatments exhibited the highest amount of micro – strain, Figure 34 and Figure 36. The samples that underwent a HIP treatment, as could be expected, exhibited the lowest amount of micro – strain in both the tensile heat treatment sample set, Figure 34, and the porosity build samples set, Figure 36. However, there is no clear correlation between the percentage of micro – strain to the percentage of relative porosity from the parameter study samples, Figure 33.

Is there any way to provide further support of the massive transformation theory? To provide evidence to the validity of a massive transformation δ-ferrite (BCC) to γ-austenite (FCC) more thermodynamic modelling is needed.

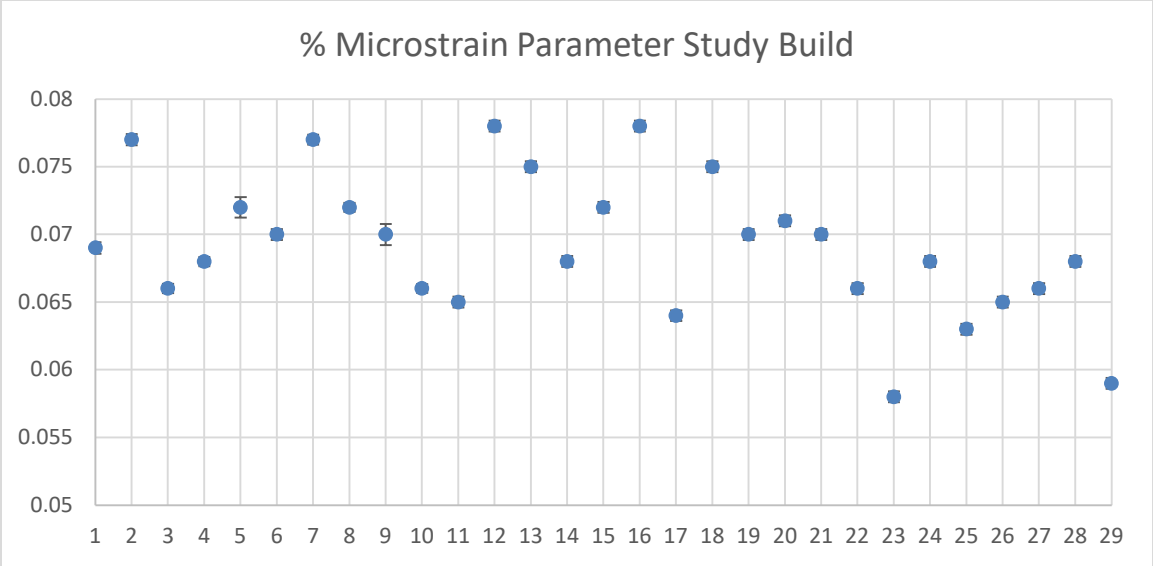


**Figure 33: Percentage of micro - strain for the parameter study samples.**

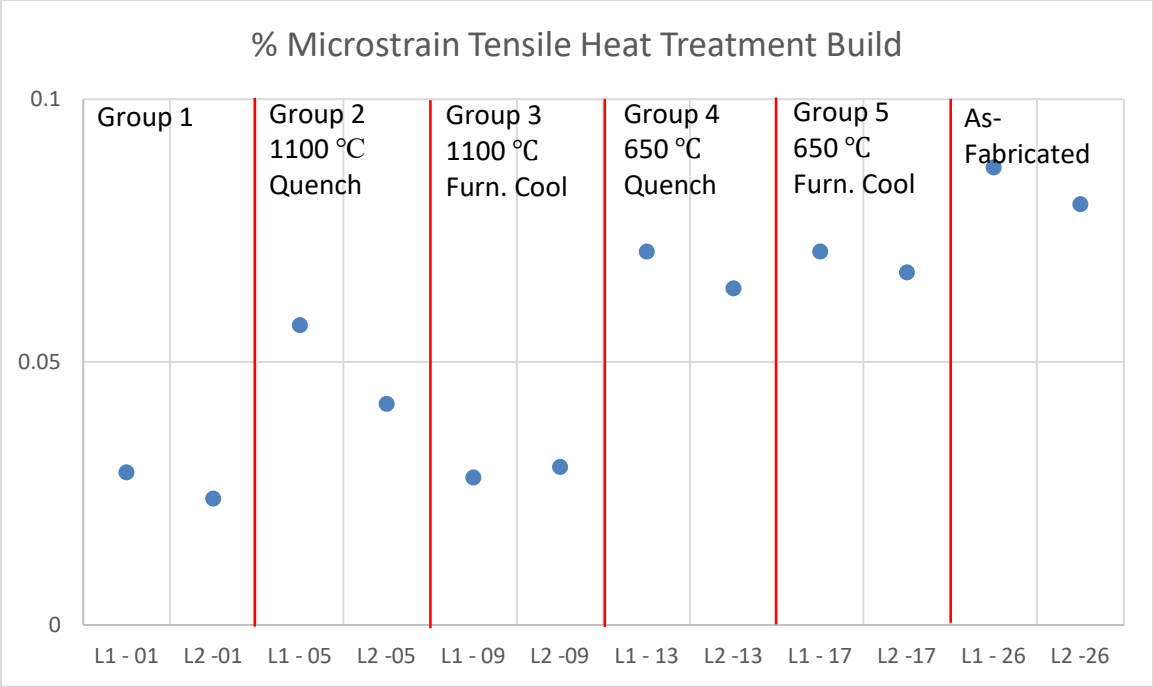


**Figure 34: Percentage of micro - strain for the tensile heat treatment study samples.**

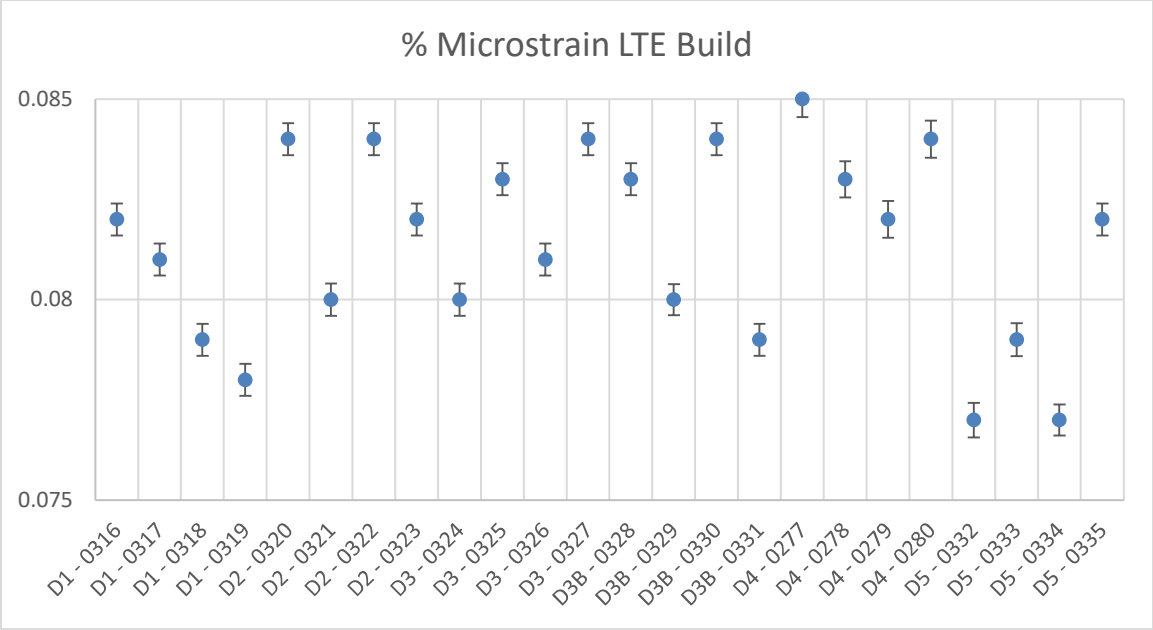


**Figure 35: Percentage of micro - strain for the LTE study samples.**

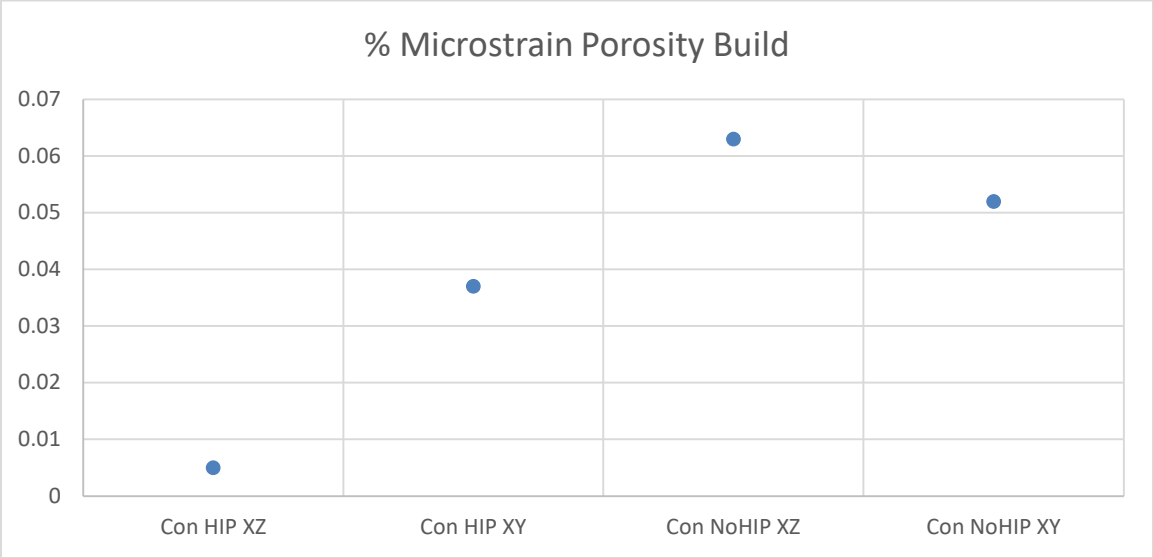


**Figure 36: Percentage of micro - strain for the porosity study samples.**

### *3.4.2 Thermodynamic Modeling – Thermocalc T – Zero Calculations*

Further thermocalc calculations were performed to provide evidence to support the theory of a massive transformation from δ-ferrite (BCC) to γ-austenite (FCC). There are two possible ways for a minimal diffusion transformation of δ-ferrite (BCC) to γ-austenite (FCC): (1) a peritectic reaction of liquid + δ-ferrite → γ-austenite or (2) a massive transformation of liquid → δ-ferrite → γ-austenite. A peritectic reaction requires complex high temperature in – situ monitoring. However, peritectic reactions are associated with low thermal gradients while massive transformations are possible with high thermal gradients as are found in this investigation. T – zero calculations performed with thermocalc provide proof of concept for the massive transformation theory. T – zero is the temperature at which the free energy of both the FCC and BCC phases are equal. The Temperature vs. Cr content plot, Figure 37, of t – zero values for various Cr contents illustrates that the initial solidification from the liquid will be the parent δ-ferrite (BCC) phase with cooling below the t – zero temperature for the given Cr (16.81 wt% for the parameter study samples) content will result in the parent δ-ferrite (BCC) phase transforming massively to the resulting γ-austenite (FCC) phase.

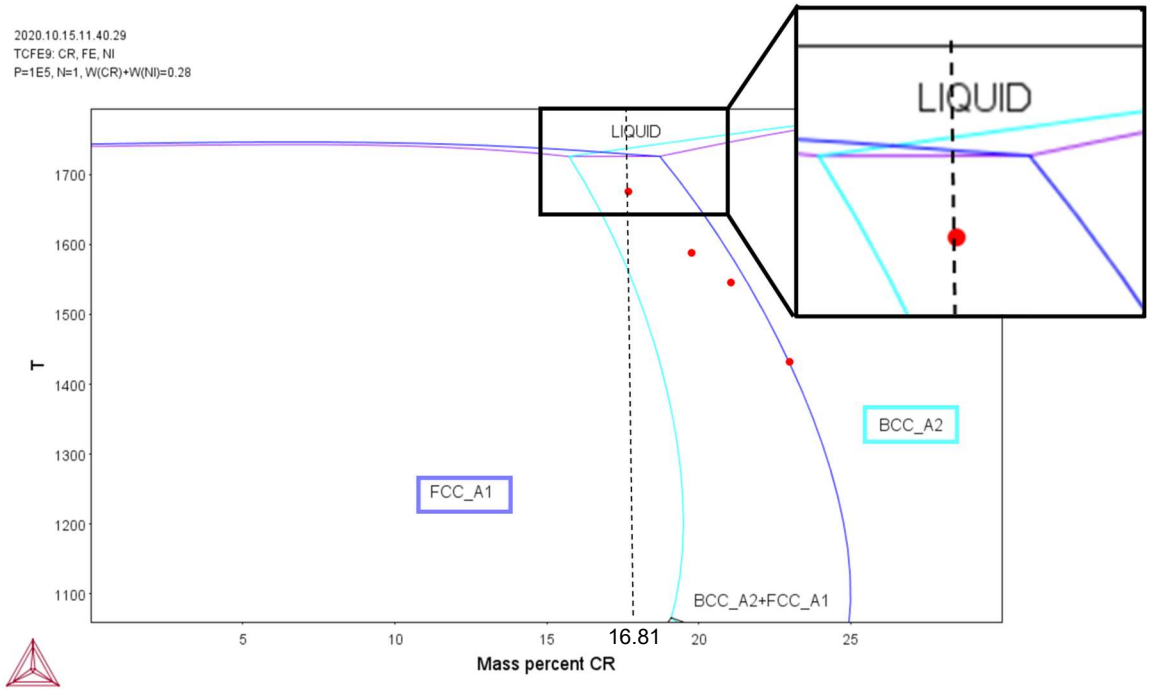


**Figure 37: T0, Cr content plot illustrating the ability of massive transformation.**

## 3.5 Theoretical Analysis of Initial BCC Solidification

This section will discuss the theoretical calculations and modelling utilized to better understand the percentage of initial solidification as δ-ferrite (BCC). Being able to predict the percentage of initial solidification of δ-ferrite (BCC) may allow for future "tailoring" of build parameters to maximize the percentage of δ-ferrite (BCC) initial solidification. This could have a meaningful impact for AM in nuclear applications. Irradiation Assisted Stress Corrosion Cracking (IASCC) is a significant issue for stainless steel components in a nuclear environment. IASCC has been shown to increase when Cr migrates to the grain boundaries [30, 31]. Thus, being able to "tailor" the amount of δ-ferrite (BCC) initial solidification in AM thereby keeping more of the Cr content in the bulk and reducing the migration to grain boundaries suggests significant potential for the reduction of IASCC.

### *3.5.1 Theoretical Modeling – SAHTM*

Further modeling was performed utilizing the Semi – Analytical Heat Transfer Model (SAHTM) developed at the MDF [11]. SAHTM models the thermal gradient and solidification velocity across a layer of a build. Each samples' build parameters were modeled and the resulting thermal gradient and solidification velocity plots for a single "idealized" weld pool was obtained for all samples. The SAHTM model for sample 6 of the parameter study may be seen in Figure 38. The solidification velocity (R) plot, Figure 38 (a), illustrates velocities moving from $10^{-2}$ m/s at the edge of the weld pool that accelerate to $10^{0}$ m/s at the center of the weld pool. The thermal gradient (G) plot, Figure 38 (b), illustrates a thermal signature of $10^{7}$ K/m at the edge of the weld pool reducing to $10^{6}$ K/m at the center of the weld pool. Such a combination of G and R values predict cellular dendritic growth during solidification as was discovered in sample 6 of the parameter study, Figure 39. To further investigate the solidification theory, post processing was performed on the solidification velocity models. A simple integration was used to predict the percentage of initial BCC solidification (lightly etching) regions for all samples. The post – processed SAHTM model for sample 6 of the parameter study is shown in Figure 40.

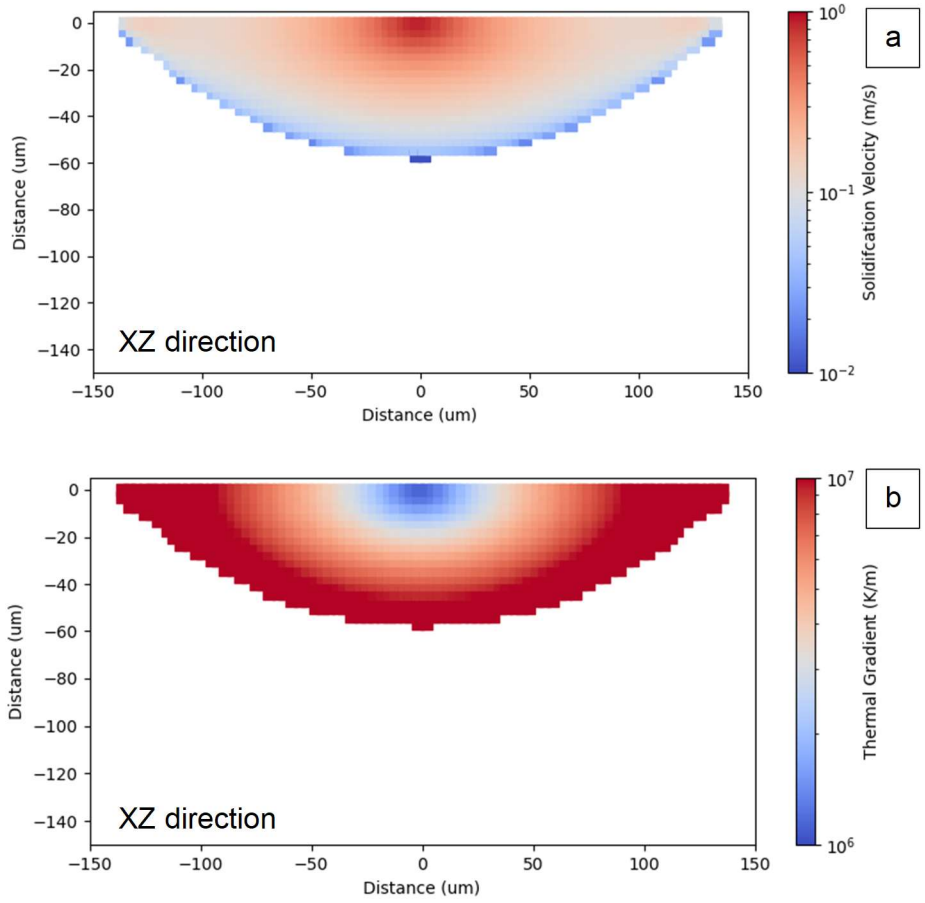


**Figure 38: Solidification and Heat Transfer Model of sample 6 of the parameter study: (a) solidification velocity and (b) thermal gradient.**

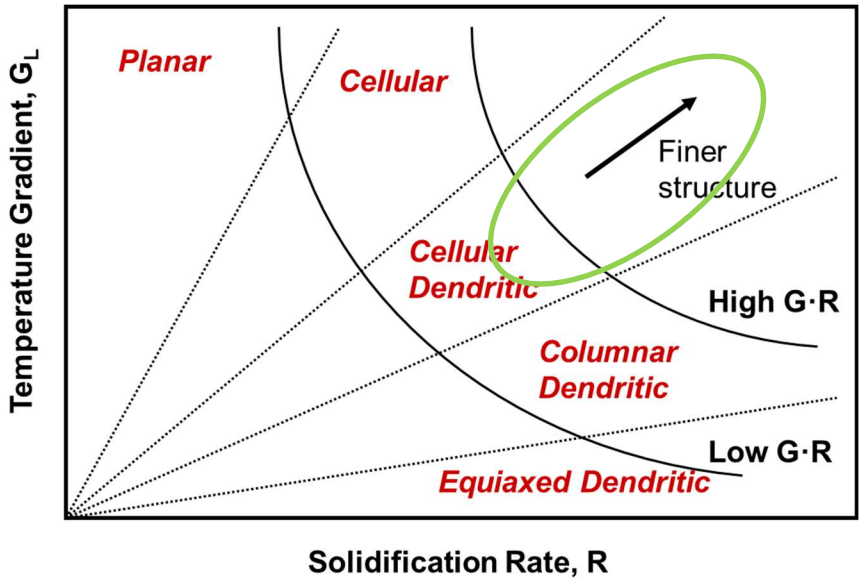


**Figure 39: Thermal Gradient (G) and Solidification Rate (R) solidification determination chart under normal welding conditions with the region of high G and high R highlighted in green.**

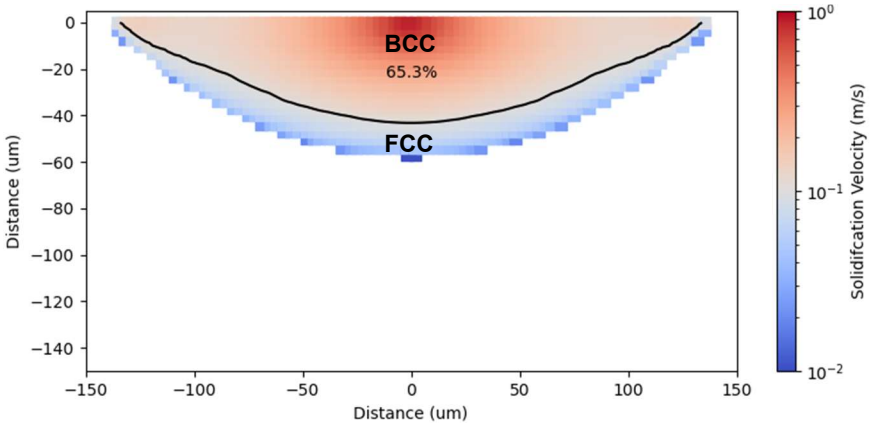


**Figure 40: Semi – Analytical Heat Transfer Model of sample 6 with post processing integration estimate of 65.3% initial δ-ferrite (BCC) solidification.**

### *3.5.2 Emerald*

A new machine learning algorithm named Emerald [32] has been developed at ORNL for automated segmentation of images based on criteria input by the user. For the purposes of this study the automated segmentation was trained to identify the percentage of darkly etched regions vs. the percentage of lightly etched regions.

Post processing of the SAHTM models allows for comparison to the percentage of lightly etched, brightly imaged regions obtained from the etched optical micrographs using the machine learning algorithm Emerald. Etched optical micrographs are segmented using the Emerald algorithm to estimate the percentage of darkly etched regions and the lightly etched regions with the lightly etched regions corresponding to initial $\delta$-ferrite (BCC) solidification. Once segmented an average was calculated over all etched images of a given sample.

For sample 6 of the parameter study the SAHTM model predicted a relative fraction of $\delta$-ferrite (BCC) initial solidification to be 65.3% with Emerald calculating 65.07% $\delta$-ferrite (BCC) initial solidification. An example of Emerald segmentation of an etched micrograph of sample 6 of the parameter study is seen in Figure 41 (b). However, Emerald was not able to accurately segment all etched micrographs as some lacked a sufficient contrast in etching. This revealed a direct dependence on the quality of etching for future analysis as the algorithm relies on the etching contrast. This means that if an etched optical micrograph lacks clear contrast, there will be more difficulty in correctly segmenting the image.

Samples from the parameter study with proper etching contrast were able to be modelled with both SAHTM and Emerald. These samples show good agreement with SAHTM predictions. The results of this comparison, Figure 42, are promising; however, more analysis will be required for full validation. The variances seen here are not of great concern considering the SAHTM model predictions presented do not account for remelting while the Emerald results are an average over several etched optical micrographs, which could account for such differences in percentage predictions.

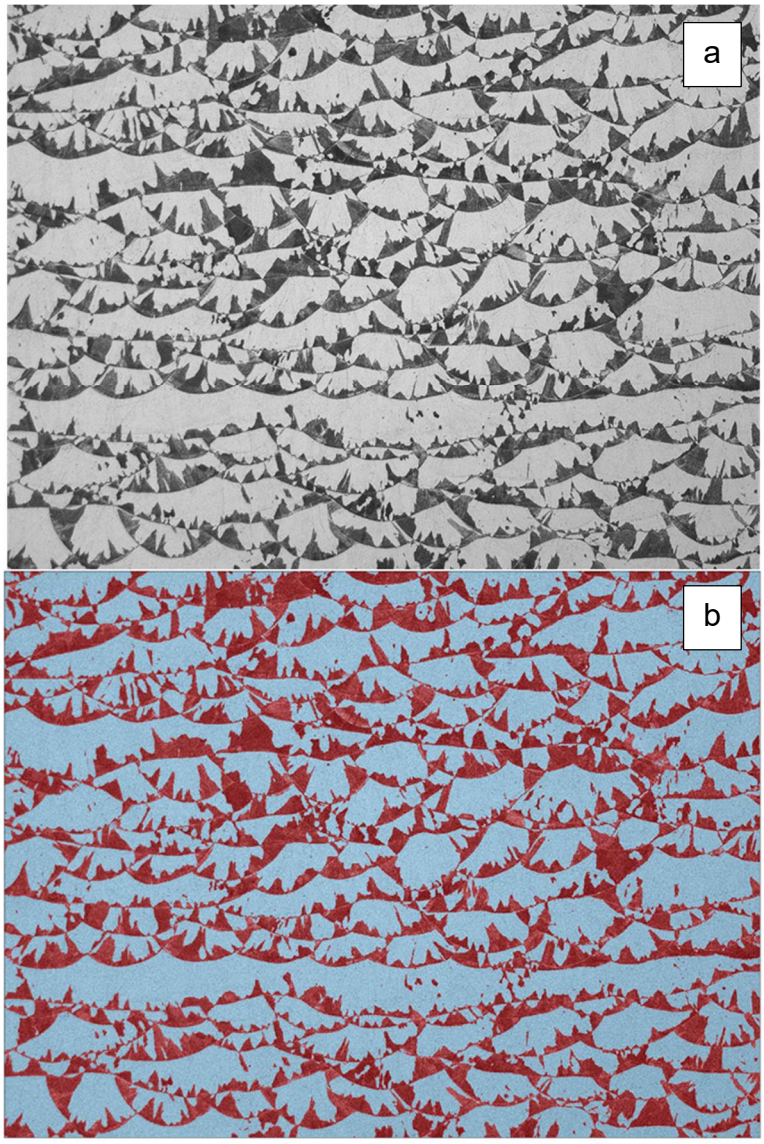


**Figure 41: Sample 6 of the parameter study: (a) etched optical micrograph and (b) Emerald segmented micrograph with the red sections indicating percentage of initial γ-austenite (FCC) solidification and the blue sections representing initial δ-ferrite (BCC) solid. Ref: Unpublished research by Simpson et al.**

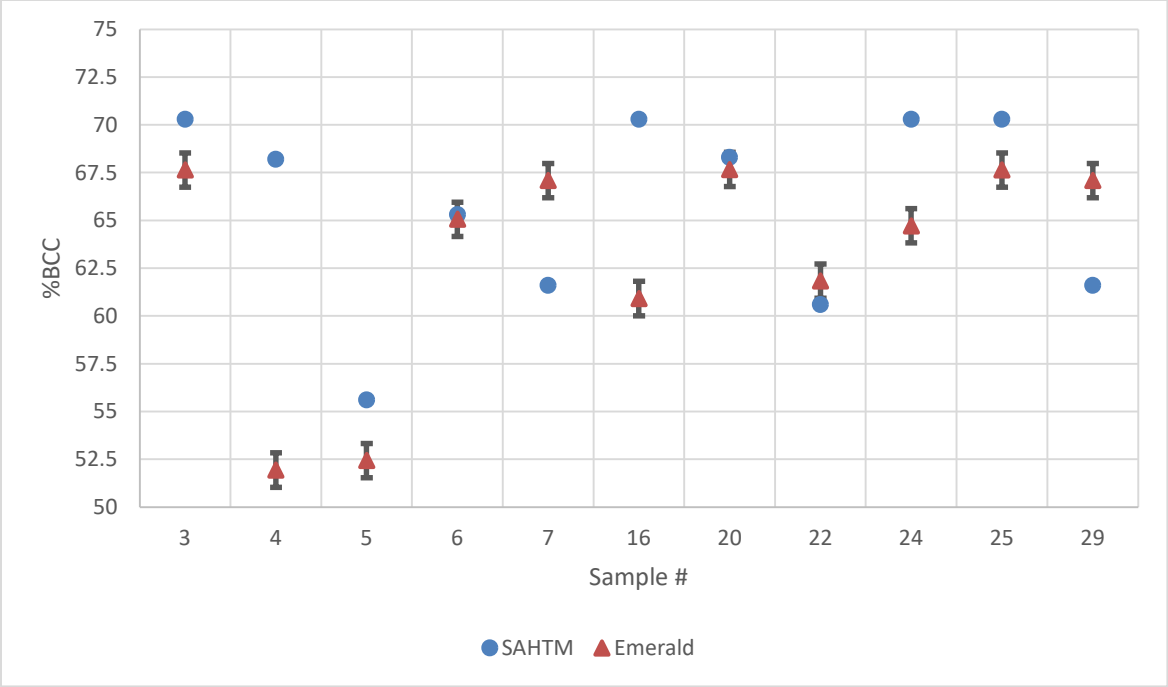


**Figure 42: Comparison of percentage of initial δ-ferrite (BCC) solidification modeled with SAHTM to that calculated with Emerald for the parameter study samples. Ref: Unpublished research by Simpson et al.**

# CHAPTER 4 SUMMARY AND CONCLUSIONS

- Nanoscale partitioning was discovered and confirmed to be the result of an abrupt transition of phase selection phenomenon from $\gamma$ - austenite (FCC) phase to $\delta$ - ferrite (BCC) phase when moving from the melt pool boundaries to the interior of the melt pool.
- This phase selection phenomena are inferred from a distinct shift in the Cr and Mo; and Ni partitioning in the inter – dendritic regions of differently etched regions of the studied samples.
- Four sample builds with varied build parameters were studied, some of which underwent heat treatments. The samples were fabricated with either SLM or Concept Laser systems.
- Nanoscale partitioning was identified and quantified in STEM/EDS samples milled from sample 6 of the parameter study.
- All samples from all four sample sets were confirmed ≥ 99% $\gamma$-austenite (FCC) through X – ray diffraction.
- Solidification models were compared to semi – analytical heat transfer models and automated segmentation through a machine learning algorithm of etched optical micrographs to predict nanoscale partitioning patterns and the percentages of such.
- The retained presence of nanoscale partitioning after massive transformation to $\geq$ 99% $\gamma$-austenite (FCC) phase was confirmed through STEM/EDS analysis as well as theoretical analysis.

These results may provide great positive impact for the use of AM in nuclear applications:

- $\delta$ - ferrite (BCC) has been shown to have a negative impact on mechanical properties, particularly in nuclear environments. However, despite $\geq$ 50% initial solidification as $\delta$ - ferrite (BCC), a significant amount of retained $\delta$ - ferrite (BCC) is not found in this study. In fact, the residual room temperature $\delta$ - ferrite (BCC) phase is ~ ≤ 1%.
- Cr that migrates to grain boundaries has been shown to significantly worsen Irradiated Stress Corrosion Cracking (IASCC) which is of great importance for internal components in a light water nuclear reactor.
- The ability to initially solidify as $\delta$ - ferrite (BCC) then undergo a massive transformation to $\gamma$-austenite (FCC) allows for the majority of Cr to remain in the bulk of a component, thereby reducing the IASCC.
- Additionally, this allows for the amount of initial $\delta$ - ferrite (BCC) solidification and the subsequent partitioning patterns to be tailored with build parameters.

# CHAPTER 5 FUTURE WORK

At the conclusion of this study, there are still several opportunities for future work. More work is needed to confirm or deny the presence and distribution of nanoscale partitioning across multiple printer types. If it can be proven that such partitioning exists across multiple print platforms, it would allow for the possibility of tailoring microstructure and nanoscale precipitates to best fit a given components expected service environment and life cycle. Thus, such future work could focus on the conformation and generalization of the solidification phenomenon through new sample set design, comprehensive characterization, as well as thorough thermodynamic and kinetic modeling.

A new sample set design could correlate the build parameters in this study in order to select optimal parameters that could, based on the findings of this study, be expected to maximize, and minimize the percentage of initial $\delta$ - ferrite (BCC) solidification. The comprehensive characterization methods could include:

- EBSD - EBSD for locating sites of interest for study.
- STEM/EDS – STEM/EDS could be utilized to confirm the solidification mode.
- Transmission Kikuchi diffraction (TKD) - TKD methods could be utilized to confirm the presence of $\delta$-ferrite.
- XRD - XRD could be performed to confirm the room temperature structure of the new build.
- Synchrotron – Synchrotron bulk analysis may be performed to confirm the percentage of elemental partitioning throughout a sample vs the surface XRD measurements collected in this study.

# References


[1] Lou, X., & Gandy, D. (2019). Advanced Manufacturing for Nuclear Energy. *Jom*, *71*(8), 2834–2836. https://doi.org/10.1007/s11837-019-03607-4

[2] Raghavan, N., Simunovic, S., Dehoff, R., Plotkowski, A., Turner, J., Kirka, M., & Babu, S. (2017). Localized melt-scan strategy for site specific control of grain size and primary dendrite arm spacing in electron beam additive manufacturing. *Acta Materialia*, *140*, 375–387. https://doi.org/10.1016/j.actamat.2017.08.038

[3] Sames, W. J., List, F. A., Pannala, S., Dehoff, R. R., & Babu, S. S. (2016). The metallurgy and processing science of metal additive manufacturing. *International Materials Reviews*, *61*(5), 315–360.

[4] Gray, G. T., Livescu, V., Rigg, P. A., Trujillo, C. P., Cady, C. M., Chen, S. R., Carpenter, J. S., Lienert, T. J., & Fensin, S. J. (2017). Structure/property (constitutive and spallation response) of additively manufactured 316L stainless steel. *Acta Materialia*, *138*, 140–149. https://doi.org/10.1016/j.actamat.2017.07.045

[5] Wang, Y. M., Voisin, T., McKeown, J. T., Ye, J., Calta, N. P., Li, Z., Zeng, Z., Zhang, Y., Chen, W., Roehling, T. T., Ott, R. T., Santala, M. K., Depond, P. J., Matthews, M. J., Hamza, A. V., & Zhu, T. (2018). Additively manufactured hierarchical stainless steels with high strength and ductility. *Nature Materials*, *17*(1), 63–70. https://doi.org/10.1038/NMAT5021

[6] Yoder, S., Nandwana, P., Paquit, V., Kirka, M., Scopel, A., Dehoff, R. R., & Babu, S. S. (2019). Approach to qualification using E-PBF in-situ process monitoring in Ti-6Al-4V. *Additive Manufacturing*, *28*(February), 98–106. https://doi.org/10.1016/j.addma.2019.03.021

[7] Yoder, S., Morgan, S., Kinzy, C., Barnes, E., Kirka, M., Paquit, V., Nandwana, P., Plotkowski, A., Dehoff, R. R., & Babu, S. S. (2018). Characterization of topology optimized Ti-6Al-4V components using electron beam powder bed fusion. *Additive Manufacturing*, *19*, 184–196. https://doi.org/10.1016/j.addma.2017.12.001

[8] Nandwana, P., Lee, Y., Ranger, C., Rollett, A. D., Dehoff, R. R., & Babu, S. S. (2019). Post-processing to Modify the α Phase Micro-Texture and β Phase Grain Morphology in Ti-6Al-4V Fabricated by Powder Bed Electron Beam Melting. *Metallurgical and Materials Transactions A: Physical Metallurgy and Materials Science*, *50*(7), 3429–3439. https://doi.org/10.1007/s11661-019-05247-4

[9] Raplee, J., Plotkowski, A., Kirka, M. M., Dinwiddie, R., Okello, A., Dehoff, R. R., & Babu, S. S. (2017). Thermographic Microstructure Monitoring in

Electron Beam Additive Manufacturing. *Scientific Reports*, *7*(January), 1–16. https://doi.org/10.1038/srep43554

[10] Nandwana, P., Kirka, M. M., Paquit, V. C., Yoder, S., & Dehoff, R. R. (2018). Correlations Between Powder Feedstock Quality, In Situ Porosity Detection, and Fatigue Behavior of Ti-6Al-4V Fabricated by Powder Bed Electron Beam Melting: A Step Towards Qualification. *Jom*, *70*(9), 1686–1691. https://doi.org/10.1007/s11837-018-3034-6

[11] Plotkowski, A., Kirka, M. M., & Babu, S. S. (2017). Verification and validation of a rapid heat transfer calculation methodology for transient melt pool solidification conditions in powder bed metal additive manufacturing. *Additive Manufacturing*, *18*, 256–268. https://doi.org/10.1016/j.addma.2017.10.017

[12] D. W. Gandy et al., "ICME and in-situ process monitoring for rapid qualification of components made by laser-based powder bed additive manufacturing processes for nuclear structural applications," *DOE-NEET-Final Report*, 2019

[13] Hensley, C., Sisco, K., Beauchamp, S., Godfrey, A., Rezayat, H., Mcfalls, T., Galicki, D., Iii, F. L., Carver, K., Stover, C., Gandy, D. W., & Babu, S. S. (2021). Qualification pathways for additively manufactured components for nuclear applications. *Journal of Nuclear Materials*, *548*, 152846. https://doi.org/10.1016/j.jnucmat.2021.152846

[14] Galicki, D., Chakoumakos, B. C., Ringer, S. P., Eizadjou, M., Rawn, C. J., Nomoto, K., & Babu, S. S. (2020). On the formation of spherical metastable BCC single crystal spatter particles during laser powder bed fusion. *Materialia*, *9*(January). https://doi.org/10.1016/j.mtla.2020.100584

[15] Puichaud, A., Flament, C., Chniouel, A., Lomello, F., & Rouesne, E. (2019). Microstructure_and_mechanical_properties_relations.pdf. 23.

[16] Tm-, O., & Vitek, M. (n.d.). *DB o327- % NATIONAL Effect of Rapid Solidification on Stainless Steel Weld Metal Microstructures and Its Implications on the Schaeffler Diagram*.

[17] Kurz, W., & Giovanola, B. (1986). *THEORY OF ~ I ~ ROSTRUCTURAL DEVELOPMENT DURING RAPID SOLIDIFICATION*. *34*(5).

[18] Vitek, J. M., & Babu, S. S. (2011). Multiscale characterisation of weldments. *Science and Technology of Welding and Joining*, *16*(1), 3–11. https://doi.org/10.1179/1362171810Y.0000000003

[19] Babu, S. S. (2009). Thermodynamic and kinetic models for describing microstructure evolution during joining of metals and alloys. In *International Materials Reviews* (Vol. 54, Issue 6). https://doi.org/10.1179/095066009X12506720908654

[20] J. A. Dantzig and M. Rappaz, "Solidification," 2nd Edition, EPFll Press, 2019

[21] D. Leonard et al., ORNL unpublished research, 2020
[22] Babu, S. S., Elmer, J. W., Vitek, J. M., & David, S. A. (2002). Time-resolved X-ray diffraction investigation of primary weld solidification in Fe-C-Al-Mn steel welds. *Acta Materialia*, *50*(19), 4763–4781. https://doi.org/10.1016/S1359-6454(02)00317-8
[23] Hilton, Z. T., Newkirk, J. W., & Malley, R. J. O. (2017). *Studying Chromium and Nickel Equivalency to Identify Viable Additive Manufacturing Stainless Steel Chemistries*. 377–386.
[24] Nishimura, T., Morishita, K., Nagira, T., Yoshiya, M., & Yasuda, H. (2015). Kinetics of the δ/γ interface in the massive-like transformation in Fe-0.3C-0.6Mn-0.3Si alloys. *IOP Conference Series: Materials Science and Engineering*, *84*(1), 0–7. https://doi.org/10.1088/1757-899X/84/1/012062
[25] Moon, S. C., Dippenaar, R., & Lee, S. H. (2011). Solidification and the δ/γ phase transformation of steels in relation to casting defects. *IOP Conference Series: Materials Science and Engineering*, *27*(1). https://doi.org/10.1088/1757-899X/27/1/012061
[26] J. M. Vitek, S. A. David, and C. R. Hinman, “Improved Ferrite Number Prediction Model that Accounts for Cooling Rate Effects-Part1: Model Development.”
[27] J. M. Vitek, S. A. David, and C. R. Hinman, “Improved Ferrite Number Prediction Model that Accounts for Cooling Rate Effects – Part 2: Model Results,” Welding Journal, 2003. [Online]. Available: file:///C:/Users/gdg/Downloads/Improved Ferrite Number Prediction Model that Accounts for Cooling Rate Effects-Part1 Model Development.pdf.
[28] Elmer, J. W., & Allen, S. M. (1989). *Microstructural Development during Solidification of Stainless Steel Alloys*. *20*(October).
[29] Byun, T., Dehoff, R., Simpson, J., & Terrani, K. (2020). *Evaluation of Heat Treatments for Additively Manufactured 316L*. 269–271. https://doi.org/10.13182/t32485
[30] Song, M., Wang, M., Lou, X., Rebak, R. B., & Was, G. S. (2019). Radiation damage and irradiation-assisted stress corrosion cracking of additively manufactured 316L stainless steels. *Journal of Nuclear Materials*, *513*, 33–44. https://doi.org/10.1016/j.jnucmat.2018.10.044
[31] Meric de Bellefon, G., Bertsch, K. M., Chancey, M. R., Wang, Y. Q., & Thoma, D. J. (2019). Influence of solidification structures on radiation-induced swelling in an additively-manufactured austenitic stainless steel. In *Journal of Nuclear Materials* (Vol. 523, pp. 291–298). https://doi.org/10.1016/j.jnucmat.2019.06.012
[32] J. Simpson et al., ORNL unpublished research, 2020

# Appendix

A. Interface Response Function (IRF) equations:

Velocity dependent partition coefficient:

$$k_V^i = \frac{k_o^i + a_o\left({}^{V_S}/_{D_i}\right)}{1 + a_o\left({}^{V_S}/_{D_i}\right)}$$

Velocity dependent liquidus slope:

$$m_V^i = m_o^i\left[\frac{1 - k_V^i\left(1 - ln\left\{{}^{k_V^i}/_{k_o^i}\right\}\right)}{1 - k_o^i}\right]$$

Dendrite tip liquid concentration:

$$c_l^{i*} = \frac{c_o^i}{1 - \left(1 - k_V^i\right)Iv\{Pe^i\}}$$

Dendrite tip temperature:

$$T_d = T_l + \sum\nolimits_i \left(c_l^{i*} m_V^i - c_o^i m_o^i\right) - \frac{2\Gamma}{R} - \frac{V_S}{\mu} - \frac{GD}{V_S}$$

Planar front temperature:

$$T_{planar} = T_s + \sum\nolimits_i c_o^i\left(\frac{m_V^i}{k_V^i} - \frac{m_o^i}{k_o^i}\right) - \frac{V_S}{\mu}$$

Where:

$k_o^i$ *is the equilibrium partition coefficient for element* $i$;
$a_o$*is the characteristic diffusion distance*;
$V_S$ *is the solid* $-$ *liquid interface velocity*;
$D_i$ *is the solute diffusivity of element* $i$;
$m_o^i$ *is the equilibrium liquidus slope of element* $i$;
$c_o^i$ *is the liquid equilibrium liquid concentration of alloy element* $i$;
$Pe^i$ *is the Peclet number for element* $i$;

$Iv\{Pe^i\}$ *is the Ivanstov function*;
$T_l$ *is the liquidus temperature of the original alloy composition*;
$\Gamma$ *is the Gibbs* $-$ *Thomson coefficient*;
$\mu$ *is the interface kinetic coefficient*.

# VITA

Amy Jordan Godfrey was born in Concord, NC, to parents Gary and Carolyn Jordan in 1974. She has one sister, Kimberly Deason; one brother, Gary Jordan Jr.; and a spouse, Andrew. Andrew and Amy have triplet daughters, Ashley, Rebecca, and Grace Godfrey. Amy graduated from Concord High School. After moving to TN, she went to Pellissippi State Community College and obtained an Associates of Science degree before transferring to the University of Tennessee Knoxville to complete a Bachelor of Science degree in Materials Science and Engineering in May of 2019. She then began as a graduate student pursuing a master's degree in Materials Science and Engineering.